FOREIGN BROADCAST INFORMATION SERVICE

JPRS Report

Science & Technology

USSR: Engineering & Equipment

19980121 198

JPRS-UEQ-90-013
13 SEPTEMBER 1990

SCIENCE & TECHNOLOGY

USSR: ENGINEERING & EQUIPMENT

CONTENTS

UDC [621.311.25:621.039]-531.9.001.24

Numerical and Theoretical Analysis of an Accelerated Load Reduction System for a VVER-1000-Equipped Power Generating Unit With Sudden Disconnection of Equipment in the Primary and Secondary Loops

[Article by I.M. Arshavskiy, C.Tech.S., V.A. Kazakov and S.B. Korolev, engineers, and A.Ye. Kroshilin, D.Tech.S., Nuclear Power Plant SRI [A-U]]

[Text] Analysis of the dynamic regimes that occur in the process of operating a power generating unit shows that some time-dependent processes involving process equipment failures can lead to serious perturbations in certain parameters with subsequent generating of a shutdown signal. The turbogenerator load shedding regime is one such process, wherein one of the two turbine feedwater pumps and two of the four main circulating pumps which operate under nominal power levels are disconnected. The primary reason for a shutdown occuring in these regimes is that reactor load reduction is too slow. Using accelerated load reduction for the power unit, which involves dropping a cluster of control rods into the core, allows us to avoid a shutdown, thereby improving the power plant's economic indicators, reducing the amplitude of thermal interactions with the equipment, and reducing the probability of a dangerous radiation leak situation as the reactor makes excursion to a critical state.

We present the results of a numerical and theoretical analysis of the efficacy of an accelerated load reduction system (ALR). We used the KIPR integrated mathematical model [1] as a tool in our investigation. We look at three separate classes of nuclear power plant operating regimes in which an accelerated load reduction system is employed.

Dynamic regimes during turbogenerator load shedding. In regimes where turbogenerator load is shed (down to no-load, internal-needs only, or zero) a strong increase in primary feedwater inlet pressure is observed, which leads to full opening of all the BRU-A atmospheric steam dump bypass valves. According to the design algorithm, in reactor load reduction one may note the following negative phenomena that accompany this class of transient:

• if certain of the steam dumps fail (either the BRU-K into the condenser or the BRU-A into the atmosphere) the reactor may be shut down because of the pressure in the steam generator;

• if the BRU-A is not closed, the reactor installation may be cooled at an unsafe rate;

• an increase in pressure in the secondary loop causes an increase in pressure in the primary loop, resulting in opening of all the spray nozzles, which is the cause of a significant drop in pressure in the primary loop during the final phase of a transient. If the spray nozzles are not activated, a scram signal is generated;

• a strong rise in temperature on the cold side;

• a high rate of steam flow into the condenser via the BRU-K steam dump may cause the turbine feedwater pump to be shut down.

Employing ALR in these regimes may either eliminate some of these phenomena, or at least significantly lessen their negative effect on the operation of the power unit. This is confirmed by the results of several numerical studies of flows in these classes of regime (taking into account possible failures during operation of the equipment) comparing the use of regular algorithms and those using ALR.

We present the results of some of these analyses (see Fig. 1). One regime corresponds to the load dropping to zero upon failure of two of the BRU-K steam dumps. The initial state of the unit corresponds to the end of a refueling cycle with a power level of 102%. This is confirmed by the Figure.

We will look now at the dynamics of a transient process as turbogenerator load is shed down to a no-load or idle condition using ALR at a nominal power level, which was realized on 7 Jun 87 on the No 3 unit of the Zaporozhe AES. The experimental and numerical results of this dynamic test are shown in Fig. 2. By plunging Cluster I into the core, in 10 s the neutron power was 52% of N_{nom} (54% of N_{nom} in the calculation). Further reactor load reduction down to 40% was carried out by a power limiter acting on Control Rod Cluster X.

A graph showing variation in pressure in the primary feedwater inlet is given in Fig. 2. The BRU-K steam dump valves began opening in proportion to the amount of load shed and were fully open after 18 s. The valves started to close at 40 s (in the experiment, 44 s) in step with the pressure drop in the secondary loop. In the experiment one of the BRU-K steam dumps failed to open as it should, and this was allowed for in the calculations. The maximum pressure in the in the primary feedwater inlet was 7.0 MPa, and 7.1 MPa in the steam generators, which is lower than that needed to trigger atmospheric exhaust via the BRU-A. In the experiment one of the BRU-As did open slightly, by 5—10%. We should note that the actual flow characteristics of the steam dumps may differ strongly from design. Thus an analysis of this regime shows that the pressure in the feedwater inlet stabilized at a level of roughly 5.9 MPa at a power level of 39% of N_{nom} and a feedwater flowrate of about 40% of G_{nom}, with three of the BRU-K valves 40% open. The feedwater temperature equalized at about 170° C. Simple calculations show that the steam flowrate in such conditions through a fully-open BRU-K is 1.20—1.35 of the design values (the lack of precision in determining the flowrate is explained by incompleteness of data about flowrates through the BRU-SN steam dump and on to the turbine as load is shed to an idle or no-load condition, as well as
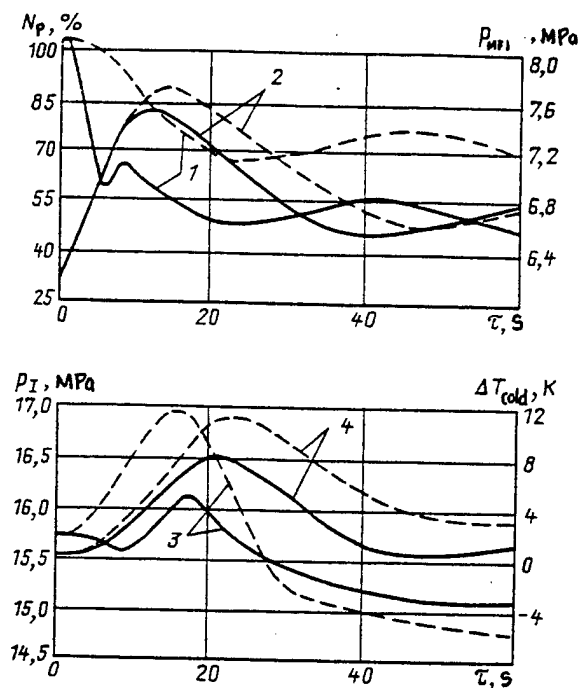
Figure 1. Graph of Variation in Parameters in the Closed SRK regime (End of Refueling Cycle, Minus Two BRU-K Steam Dumps): 1-Neutron power; 2 and 3-pressure in main feedwater inlet and pressurizer; 4-temperature on the cold side (solid line, ALR in use; dashed line, ALR not in use)

2
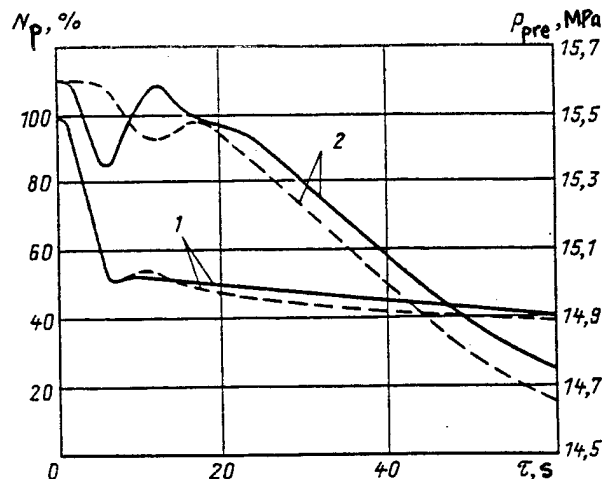
Figure 1. Graph of Variation in Parameters in the Load Shedding Regime Down to No-Load at the Zaporozhe AES: *1*-Neutron power; *2* and *3*-pressure in main feedwater inlet and pressurizer; *4*-temperature on the cold and hot sides; *6*-mean temperature in the primary loop (solid line is experiment, dashed line is calculation)

incompleteness of data on the degree of nonlinearity of the BRU-K valve flowrate characteristic curve). When performing the calculations for this regime the flowrate through the open BRU-K was taken to be $1.25 \ G_{design} = 1125$ t/h.
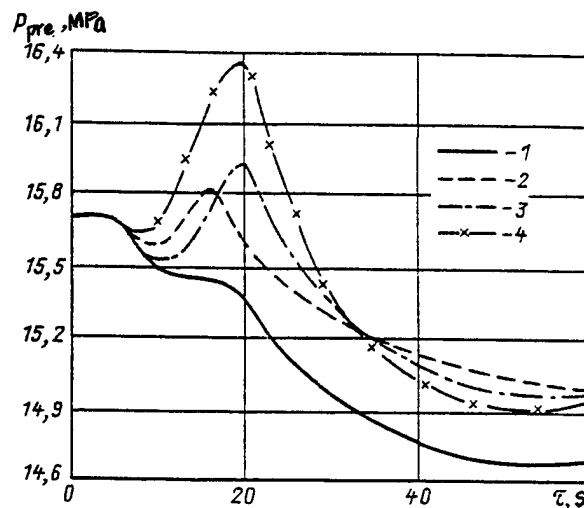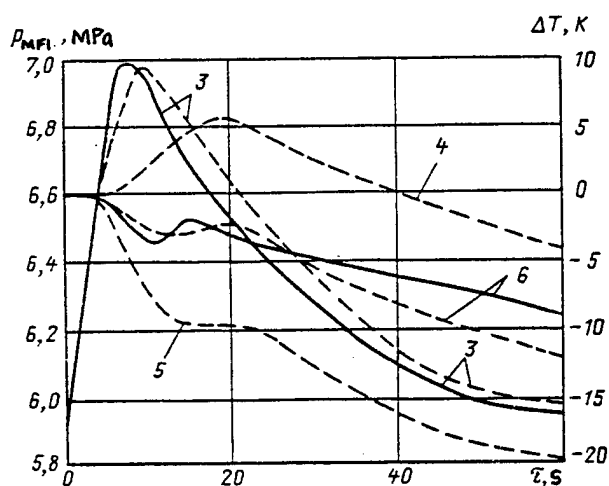
This analysis shows that using ALR and opening the BRU-K in proportion to the load shed in this regime, even when one of the BRU-K fails, will ensure that enough pressure is maintained to keep the BRU-A closed (one BRU-A opened by a total of only 5—10%) and allows us to avoid opening up the pressurizer spray nozzles during the transient.

The good agreement between experimental and calculated results confirms that the KIPR

Figure 3. Calculated Curves of Variation in Pressure in Pressurizer (*a*) and Main Feedwater Inlet (*b*) in the Closed SRK Regime Using ALR: *1*-Start of a refueling cycle, all steam dumps operating; *2*-End of a refueling cycle, all steam dumps operating; *3*-Start of a refueling cycle, minus four of the BRU-K steam dumps; *4*-end of a refueling cycle, minus four BRU-K steam dumps

3

integrated software package is accurate to a satisfactory degree, and lets us carry out numerical analysis of a number of other possible variants in the flows of other regimes that employ ALR.

The following variants were examined:

1. Load shedding down to zero; start of a refuel cycle; all steam dumps in operation.

2. Load shedding down to zero; start of a refuel cycle; four of the BRU-K steam dumps fail.

3. Load shedding down to zero; end of a refuel cycle; all steam dumps in operation.

4. Load shedding down to zero; end of a refuel cycle; four of the BRU-K steam dumps fail.

In carrying out the calculations the flowrate through the steam dumps was taken to be 1125 t/h at a pressure of 6.28 MPa. A curve of the variation in pressure in the primary and secondary loops in this regime is shown in Fig. 3. From analysis of the curve we may draw the following conclusions:

• at the beginning of a refuel cycle no opening of the spray nozzles in the pressurizer was observed. Thus, even when four of the BRU-K steam dumps fail the maximum pressure in the primary loop exceeds the initial pressure by only 0.28 MPa, and does not reach a level where the spray nozzles are operated. At the end of a cycle (in variant 4) both spray nozzles are opened (by 84 and 50% respectively) and the maximum pressure in the pressurizer is 16.35 MPa at 20 s. However, if they fail this does not lead to a shutdown; the pressure must increase to 17.3 MPa for this to happen.

• in all regimes the minimum pressure in the primary loop is no lower than 14.5 MPa;

• at the beginning and at the end of a refuel cycle, with all steam dumps operating, the pressure in the main feedwater inlets is not more than 1.25 MPa. There was a momentary opening of the BRU-A observed; in variant 1, by 26% and in variant 3, by 34%. We note that if the initial pressure in the feedwater inlet was 5.88 MPa (60 kgf/cm^2), which is what occured in the dynamic regime we looked at earlier, then there is no opening of the BRU-A;

• when all four BRU-K fail, all the BRU-A open fully. The maximum pressure in the main feedwater inlet (and in the steam generators, since in these variants they are approximately the same) is: in regime 2, 2.68 MPa and in regime 4, 7.74 MPa, which is quite near shutdown pressure level for the steam generator of 7.85 MPa.

Dynamic regimes with one of two operating turbine feedwater pumps disconnected. Disconnection of one of the two operating turbine feedwater pumps results in serious perturbations in the feedwater flow to the steam generator, and thus the primary problem in this process is to maintain a nominal water level in the steam generator.

At nominal power levels, a shutdown results if this regime runs its course (either from the 500 mm drop in level in one of the steam generators, or from the fact that two of the operating main circulation pumps are disconnected, causing a 200 mm drop in level in the corresponding steam generators). Accelerated load reduction of the unit makes it possible to rapidly reduce the thermal flux to the steam-water mixture in the steam generator from the primary loop side, and thus to lower the steam flowrate from the steam generator and reduce the imbalance in feedwater and steam flowrates, which is the primary reason for the sharp drop in water levels in the steam generators.

However, dropping a rod cluster in this regime results in a pressure drop in the main feedwater inlet, if the EGSR turbine regulator is in the operating regime for maintaining a nominal steam pressure before the turbogenerator SRK valve throughout the transient process. Thus we need a different algorithm for reducing the load on the turbine. Initially we proposed the following:

- reducing the load on the turbine by 150 MW in the first 1 s; and

- further reducing the load down to 500 MW at a rate of 15—20 MW/s.

Analysis of the regime in which one of two operating turbine feedwater pumps is disconnected, and ALR is employed, is carried out using the experimental and numerical results from two dynamic tests performed on VVER-1000 power generating units.

Regime 1 was carried out on 28 Jan 89 on the No 2 unit of the South Ukraine AES at the end of a refueling cycle (270 eff. days).

Regime 2 was carried out on 29 May 87 on the No 3 unit of the Zaporozhe AES at the start of a refueling cycle (127 eff. days).

The initial algorithm for turbine load reduction was employed, and in the experiment the EGSR regulator was in the "process safety" mode when after 1 s the turbine load was reduced by 160 MW and thereafter at a rate of 10 MW/s down to a level of 500 MW (38 s into the process), after which the turbine went into the RD-1 regime with a regulator setting of 6.0 MPa. The inital turbogenerator load reduction led to an increase in the pressure at the main feedwater inlet and the activating of the BRU-K valves. Three BRU-K valves were 20% closed 15 s into the transient. The pressure in the feedwater inlet reached its maximum value of 6.45 MPa at 26 s, after which it fell in proportion with the thermal power of the unit and the operation of the steam dumping equipment.

As has already been noted, defining the EGSR turbine regulator operating algorithm is the most important step in implementing ALR. The initial algorithm leads to an increase in pressure in the main feedwater inlet and opening of the BRU-K, which is undesirable because of possible failures of these regulators. A sharp drop in pressure at the feedwater inlet is also inadmissible. The best thing would be a turbine load reduction algorithm such that the pressure at the feedwater inlet is maintained somewhere in the range $p_{nom} \pm 0.2$ MPa.

An optimal turbogenerator load reduction algorithm in a regime where one of the two operating turbine feedwater pumps is shut off was selected on the basis of a multivariate calculation using the KIPR software package. It assumes that the EGSR regulator operates during this transient in a regime that maintains steam pressure before the turbine (RD-1), however, this pressure is variable and is determined from the graph in Fig. 4.

This algorithm was implemented in regime 2 (Fig. 5). Within 1.4 s after disconnecting turbine feedwater pump TFP-2 a signal was sent to activate power limiting and drop the first control rod cluster. Turbine load reduction occurred at the same time as reactor load reduction. Upon a signal for accelerated load reduction to the EGSR the RD-1 pressure maintainance regime was activated and within 4 s that steam pressure began to change in accordance with the selected algorithm (Fig. 4). Turbine load reduction was initiated after 6 s and was terminated at 37 s by a false switching of the automatic output power regulator to the T regime and of the EGSR to the regime where turbine power is kept constant at 660 MW (for a reactor power of 49%). This was taken into account in performing the numerical calculations for this regime. The imbalance in reactor and turbine power led to a drop in pressure at the main feedwater inlet. However, the good agreement between the numerical and experimental pressure behavior at the feedwater inlet up to the 37 s point allows us to conclude that, were it not for the false switching of the EGSR taking it from the RD-1 regime, the pressure at the feedwater inlet could have been maintained within the prescribed limits. Fig. 5 shows the numerical behavior of the pressure at the feedwater inlet for precise implementation of the selected algorithm.

Figure 4. Graph of Variation of Pressure Setting in Turbine EGSR Regulator

Figure 5. Graph of Variation in Parameters in the Regime Where One Turbine Feedwater Pump is Disconnected at the Zaporozhe AES: *1*-Electrical power; *2* and *3*-Flowrates of feedwater to and steam from steam generator; *4*-pressure in main feedwater inlet; *5*-level in steam generator (solid line is experiment, dashed line is calculated, dash-dot line is calculated while observing EGSR algorithm)

From analysis of the regime where one of two operating turbine feedwater pumps is disconnected, we may conclude the following:

• ALR in this regime allows us to avoid shutdown because of reduced water levels in the steam generator;

• the selected algorithm for EGSR regulator operation ensures that the pressure at the feedwater inlet will be maintained within the prescribed limits.

Dynamic regimes when two of the four operating main circulating pumps are disconnected. Regimes in which various numbers of the main circulating pumps are disconnected involve a decrease in coolant flowrate through the core. The absence of DNB over the fuel rod surface is the criterion for reliable core cooling. The output power limiter reduces reactor load down to 67% N_{nom} to meet this criterion when one of the four main circulating pumps is disconnected. If two of the four main circulating pumps are disconnected (either simultaneously or within a period of time of less than 70 s) then, as designed, a shutdown signal is sent. This is because if the shutdown signal were not sent, DNB could arise 13 s into the process (according to calculations using the Dinamika program [2]) over maximumally thermal-stressed fuel rods for an adverse, albeit possible, combination of parameters. As we will show further on, using accelerated load reduction of a unit in the regime where two main circulating pumps are powered down lets us avoid DNB and, consequently, the need for a shutdown.

The results of processing the data from dynamic tests where two of four operating main circulating pumps are disconnected using ALR, as carried out on 4 Jun 87, at the No 3 unit of the Zaporozhe AES, are shown in Fig. 6. As the two pumps were disconnected, after 1.4 s the power limiters were activated and a signal was sent to drop the first cluster of scram rods. Twenty-five seconds into the transient the control rods had reduced the reactor load down to 49%, and the automatic output power regulator was connected to control it. As a result of the increased pressure at the feedwater inlet (by roughly 1.5 bar) the output power regulator was switched over to the T regime (maintaining the pressure in the secondary loop) and
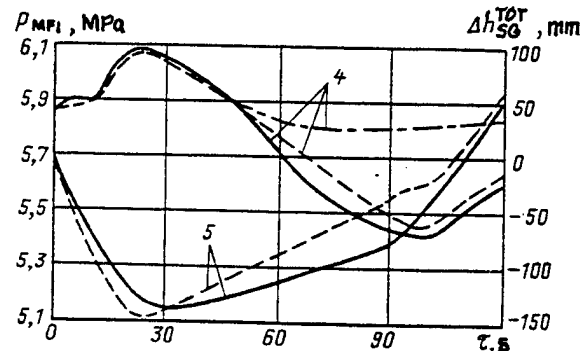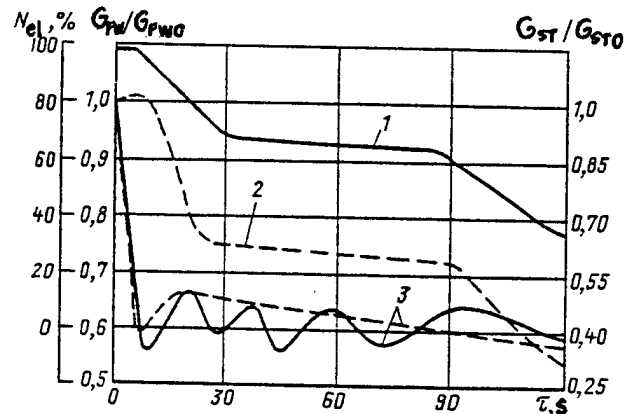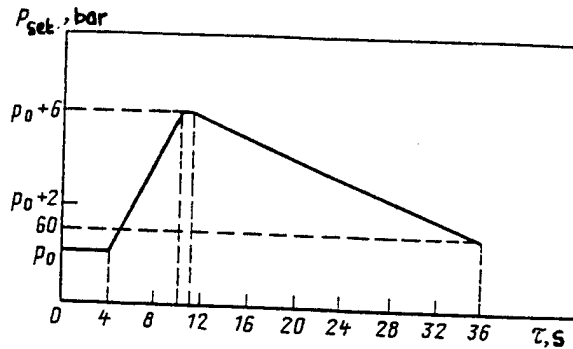
Figure 6. Graph of Variation in Parameters in the Regime Where Two Main Circulating Pumps are Disconnected at the Zaporozhe AES: *1* and *2*-Electrical and neutron power; *3*-Flowrate through the core; *4* and *5*-pressure in the pressurizer and the main feedwater inlet (solid line is experiment, dashed line is calculated)

reactor load was reduced down to 36% of N_{nom}. Upon a signal from the ALR to the EGSR the RD-1 regime was engaged and preset variation in pressure as per Fig. 4 was initiated. This EGSR operating algorithm ensured that the pressure in the primary and secondary loops is maintained within permissible limits.

Disconnection of two of four operating main circulating pumps is accompanied by a reduction in the flowrate through the core (Fig. 6) and the danger of a breakdown in reliable core cooling conditions. However, dropping in a cluster of rods leads to a sharp decline in power output and a reduction in the thermal flux coming off the fuel rod surfaces. As a result η, the safety margin to DNB, defined as the ratio of current thermal flux to critical thermal flux under the given conditions for a maximally-thermal stressed fuel rod, remains greater than unity over the course of the entire process. The minimum value of η is 1.49 at roughly 2.2 s (the stationary value was 1.525). We should note that the critical thermal flux calculations were performed according to the methods in [3,4], the shape of the neutron field and the coefficient of nonuniformity over the core volume were taken from the calculations of the Dinamika software, and the rest of the parameters are experimental.

In order to obtain a conservative estimate of the minimum safety margin to DNB η in the regime where two main circulating pumps are simultaneously disconnected, we performed calculations for the most adverse combination of unit parameters. The initial conditions were as follows: $N = 107\%$ of N_{nom}, $P_{pressurizer} = 15.4$ MPa (157 kgf/cm^2), $P_{feedwater\ inlet} = 6.08$ MPa (62 kgf/cm^2), and flowrate through the reactor $G = 80,000$ m^3/h. The shape of the neutron field and the coefficient of its nonuniformity were taken from [2], and the delay before dropping a cluster of control rods was 1.65 s.

The results of the appropriate calculations show that, for this kind of combination of parameters, η for a thermally-stressed fuel rod remains substantially greater than unity. The minimum value of the coefficient η_{min} was 1.36 at 2.1 s; the initial value was 1.394. The calculations we performed have demonstrated that when two of the main circulating pumps are simultaneously disconnected, using ALR ensures reliable reactor core cooling.

We examine now the regimes in which two of the main circulating pumps are disconnected one after the other. When the first is disconnected it sets off the PZ-1 signal, and the power limiters begin reducing reactor load by dropping a control rod cluster into the core. After the second main circulating pump is disconnected (if the interval of time between disconnection of both pumps is less than 70 s) the first
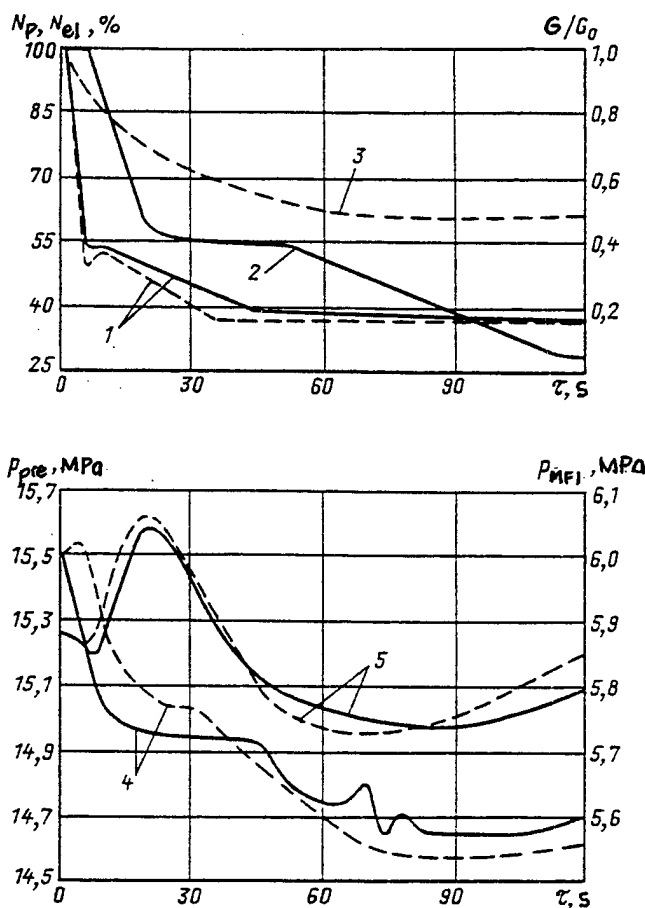
cluster is lowered into the core after a delay of 1.65 s. In the calculations we analyzed the regime where two main circulating pumps were successively disconnected in an interval of between 5 and 70 s. The initial conditions of the unit and the neutron physics properties of the core correspond to that described earlier. From the standpoint of ensuring reliable core cooling, the most dangerous regime is that in which the delay in disconnecting the second pump is $\Delta\tau = 18$ s, because when the first pump has been disconnected and the power limited activated the minimum value of the coefficient η is reached 18 s into the transient. However, even in this case η remains substantially greater than unity.

In the $\Delta\tau = 10$ s regimes no excursion of the unit parameters beyond permissible limits was noted, with the exception of a combination of the disconnected pumps. The calculations show that if we first disconnect the main circulating pump for the loop connected to the pressurizer (the fourth loop in an actual unit), then the shutdown triggering point is reached on account of the drop in pressure in the primary loop. The results of modelling this regime are given in Fig. 7. The principal reason for the drop in pressure in the primary loop to the shutdown triggering point of 13.73 MPa (140 kgf/cm^2) is the massive reactor load reduction following the lowering of the control rods as a result of a PZ-1 signal being generated from the temperature on the hot side (because of a large influx of saturated water from the pressurizer as compared to underheated water from the VKS).

This adverse effect of a strong increase in temperature on the hot side is manifest only for this combination of connected pumps and with a delay in disconnecting the main circulating pumps of 5 s $< \Delta\tau < 20$ s. For $\Delta\tau < 5$ s the flowrate through the fourth loop at the moment ALR is engaged is adequate and the inflow of coolant from the pressurizer does not lead to a strong increase in temperature on the hot side. Similarly, for $\Delta\tau > 20$ s a reverse flow of coolant in these loops precludes an increase in temperature and, consequently, the prophylactic safety measures that are the cause of the massive reactor load reduction.

Calculations for the $\Delta\tau = 60$ s regime show that ALR is engaged the moment the power limiters reduce the reactor load down to a power level of 75—80% of nominal, which may lead to setting off a shutdown from the lowering of the pressure in the primary loop.

A numerical and experimental analysis of the regimes in which two of four operating main circulating pumps are disconnected using ALR allows us to draw the following conclusions:

• an operating algorithm for the EGSR turbine regulator selected on the basis of these calculations
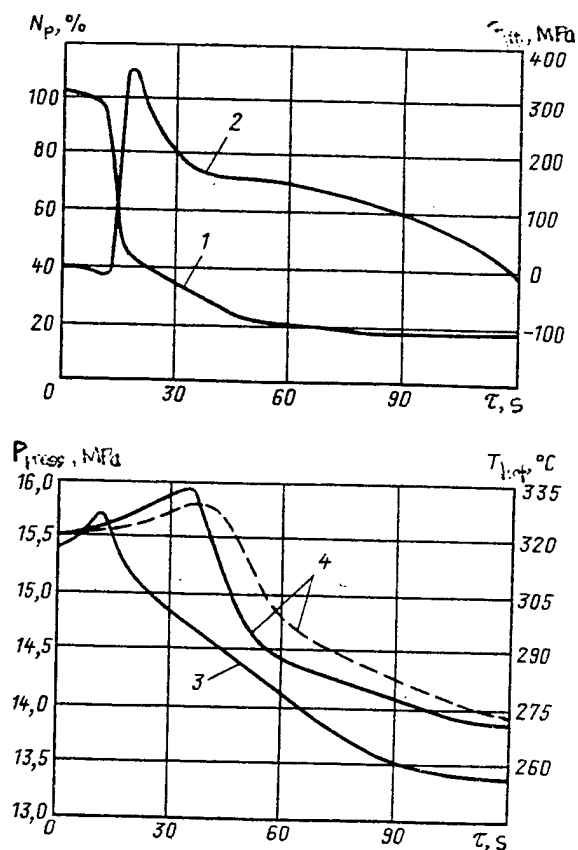

Figure 7. Calculated Curves of Variation in Parameters in the Regime Where Two Main Circulating Pumps are Disconnected With a Delay of 10 s: 1-Neutron power; 2-Flowrate Through DT ($G > 0$ upon leaving pressurizer); 4-pressure in pressurizer; 5-Hot side temperature (solid line is actual, dashed line is taking into account delay in thermocouple readings)

8

will maintain unit parameters within permissible limits, which is confimrmed by the results of dynamic tests in which two of the main circulating pumps were simultaneously disconnected;

• reliable core cooling is ensured in all regimes, even for adverse combinations of regulator parameters;

• in two cases two of the main circulating pumps are disconnected one after the other a shutdown is possible due to an increase in the temperature of the primary loop, which causes a massive reactor load reduction during the transient. In the first case, in which the delay until disconnecting the second pump in in the 5—20 s range (and the pump connected to the pressurizer is disconnected first), this is associated with the temperature on the hot side setting off a PZ-1 signal. In the second case, in which the second pump is switched off within 50 to 70 s after disconnection of the first, this is associated with a reduced neutron power and pressure in the primary loop at the moment ALR is engaged. In all other cases, including simultaneous disconnection of pumps, no tripping of the shutdown was noted.

Thus the results of a detailed numerical analysis of the dynamics of a power generating unit in regimes where ALR operates shows the advisability and efficacy of its use. The numerical study allows us to refine unit regulating system algorithms and to study the dynamics of regulators over a broad range of operating regimes.

Bibliography

1. Arshavskiy I.M., Dmitriyev V.M., Korolev S.B. and Kroshilin A.Ye. "The KIPR integrated package of time-dependent programs for studying the dynamics of VVER-1000-equipped nuclear power plants", ELEKTRICHESKIYE STANTSII No 2 1990

2. Spasskov V.P., Volkov G.A., Volkov V.A. et al "Program for the BESM-6 computer: calculation of time-dependent regimes in VVER-eqipped power generating installations" in "Dinamika. 1776/OFAP 1978" Nos 3, 4, Moscow, TsNIIAtominform, 1979

3. Bezrukov Yu. A. et al, "Doklad na vtorom tepolofizicheskom seminare stran-chlenov SEV 'Tepolofizicheskiye issledovaniya dlya obespecheniya nadezhnosti i bezopasnosi yadernykh reaktorov tipa VVER'" [A Speech to the Second Thermal Physics Seminar of CEMA Member-States "Thermal Physics Studies For Ensuring Safe and Reliable Operation of VVER-Equipped Nuclear Reactors"], Budapest, March 1978

4. Smolin V.N., Mironov Yu.V., Polyakov V.K. and Shpanskiy S.V. "Experimental study and methods for calculating DNB in reactor channels" in "Voprosy atomnoy nauki i tekhniki. Ser. Fizika i tekhnika yadernykh reaktorov" [Issues in Nuclear Science and Technology. Series Physics and Technology of Nuclear Reactors], No 1 (30), Moscow, TsNIIAtominform, 1983

UDC [621.311.25:621.039]:621.65.001.42

A Study of the Dynamic Characteristics of Pump Sets in the Process Water Supply System of an AES Power Generating Unit Under Operating Conditions

[Article by S.G. Belyayev, C.Tech.S. at the Leningrad Polytechnic Institute, and A.I. Puzanov, V.P. Belikov and B.S. Disik, engineers at the Ignalinsk AES]

[Text] The operating reliability of an AES power generating unit in large measure depends on uninterrupted operation of the process water supply system that ensures supply of water to the primary and secondary entities of the generating unit, including:

• the process condensers;

• systems for cooling bearing assemblies in the equipment;

• reactor cooling systems;

• coolant loops in the emergency system channels of the reactor;

• heat exchanger apparatus in the ventilation and water treatment systems, etc.

The safe operation of the reactor installation in an AES in large part depends on the reliable operation of all subassemblies in the process water supply system (PWSS), in particular during transient and emergency unit operating regimes[1].

A PWSS is an extensive branched hydraulic network; one of its basic features is the differing requirements imposed by the different consumers in terms of flowrates and water pressure. It is assumed that these hydraulic network operating regimes are such that the total flowrate to consumers fluctuates in the range from 2.47 to 10.28 m^3/s. In addition, there are seasonal fluctuations in flowrates.

The most important subassembly in a PWSS is the pumping equipment that supplies water to the network from a reservoir. Ensuring the reliability and proper operation of a pump set is a priority problem[2]. However, quite often the operating conditions are examined without reference to its connection with the operation of the hydraulic network. Notably, the performance range of an individual pump is hardly monitored at all during the monitoring of PWSS parameters.

We investigated a 1000V-4/63 pump set. Analysis of the results of our observing the operation of pumps at two AES power units shows that the range of water delivery covers the entire performance range of operating characteristics (from 2 to 3.2 m^3/s), and when several pumps operate together in the network their delivery rates are usually different.
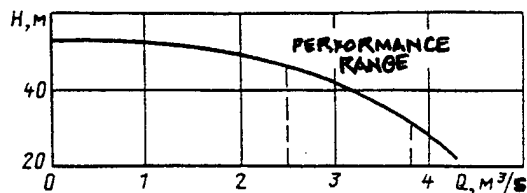
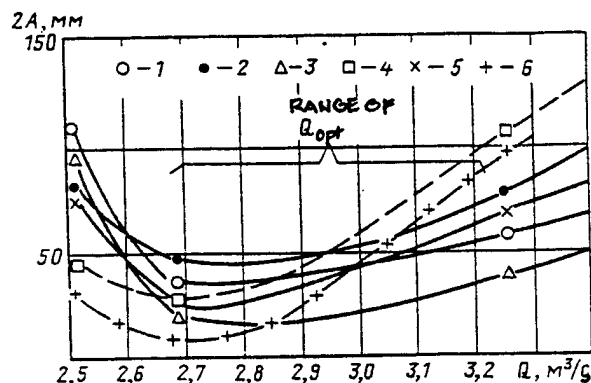Figure 1. Performance Characteristic Curve for a Centrifugal Pump in a PWSS

Figure 2. Graph of Vibration in Lower Bearings as a Function of Operating Regime: *1*, *2*, *3* are 2, 2.5 and 4 Hz; *4* is the rotation frequency; *5* is twice the rotation frequency; *6* is the blade frequency.

If we look at a pump characteristic curve (see Fig. 1), in certain cases we note regime points that go beyond the performance limits. This becomes possible because the useful part of the pump head characteristic curve, especially at low deliveries, is gently sloping and either variations in the operating regime of the network or of individual differences in pump head and the resistance to this head in the lines has a substantial impact on the location of the pump regime points on the operational characteristic curve. In turn it was found that the excursion of a pump from the performance range is characterized by a sharp increase in dynamic load acting on the pump set housing and its supports: vibration increases, as does the intensity of hydrodynamic pressure pulsations. It was found that pump housing vibration when the regime departs from the performance range may be triple the level of vibration relative to normal operating conditions.

One of the necessary conditions for correct operation of centrifugal pump sets during their operation in complicated hydraulic networks is the timely determination of the quantitative and qualitative dependences of dynamic loading on the operating regimes of the pumps themselves and the PWSS.

to discover these dependences we studied both the dynamic characteristics of pumps and certain of the process parameters: flowrate and pressure in PWSS pressurized lines, pressure in the pump discharges, and the current draw of the electric drive motors.

Vibration pickups were mounted onto the intake pipes, the lower guide bearings and the drive motor housing. The hydrodynamic pressure was measured in the region below the pump impeller, in the transits of the spiral case, and at the discharge pipe. The measurements were performed using domestic vibration measuring equipment, the VI6-6TN in combination with a DD-6S pressure pickup and DU-5S vibration accelerometer, as well as some equipment from Bruell and Kerr: a 2120 spectrum analyzer and 2305 printer. A study was made of three operating regimes with variation of flowrate in the network from 2.47 to 3.17 m^3/s. The operating parameters of the pump aggregate during the tests in the three operating regimes are given below.

	A	B	C
Flowrate	3.17	2.64	2.47
Pressure in the pressurized lines, mH_2O	4.6	5.2	5.4
Electric motor current load, A	185	160	150
Maximum amplitude of housing vibration, 2A, μm	60	35	110

As a result of the dynamic studies of the pump sets we found not only the maximum vibration in the elements, but also found the frequency range of vibrational loads. It turned out that these vibrational loads were characteristic ones in the frequency spectrum: $f_1 = 2$ Hz, $f_2 = 2.5$ Hz, $f_3 = 4$ Hz, $f_4 = 5.33$ Hz

11

(f_{rot}), $f_5 = 10.66$ Hz $(2f_{rot})$, and $f_6 = 31.98$ (f_{blade}), where f_{rot} is the rotation frequency and f_{blade} the blade frequency.

Fig. 2 shows a graph of the variation in peak-to-peak amplitude of vibrations (2A) at the characteristic frequencies as a function of the operating regime of the pump. We note that in regime A, i.e. an increase in flowrate, a maximum in the vibration of the lower guide bearing was recorded at $f = f_{rot}$ and $f = f_{blade}$. Vibration at lower frequencies were considerably less. In the optimal flowrate zone (regime B) vibration was registered to be at the same level for almost all of the characteristic frequencies with some increase in amplitude at $f = 2$ Hz and $f = 2.5$ Hz. For pump operation in regime C, i.e. decreasing delivery, there is a redistribution of the dominant frequencies in the spectrum. The greatest vibration is noted at low frequencies below the rotation frequency. Thus when the pump is in operation with a flowrate of less than $Q = 2.64$ m^3/s the possibility of low frequency vibration (2 to 4 Hz) goes up sharply, which makes the major contribution to the integral dynamic load acting on the housing and support elements of the pump set, which may be a cause of equipment breakdowns and failures.

Long-term observation of pump operation has shown that when pump delivery is reduced to that corresponding to a current draw of the motor of less than 150 A, the vibration, noise and level of hydrodynamic load increase noticeably.

We may note that, on the basis of spectral analysis of the hydrodynamic pressure pulsations at the walls of the spiral case, in all the studied regimes most of the pulsational load energy is transmitted at those frequencies for which an increase in pump housing vibration was recorded. In addition, a significant part of the energy was transmitted at triple the rotational frequency.
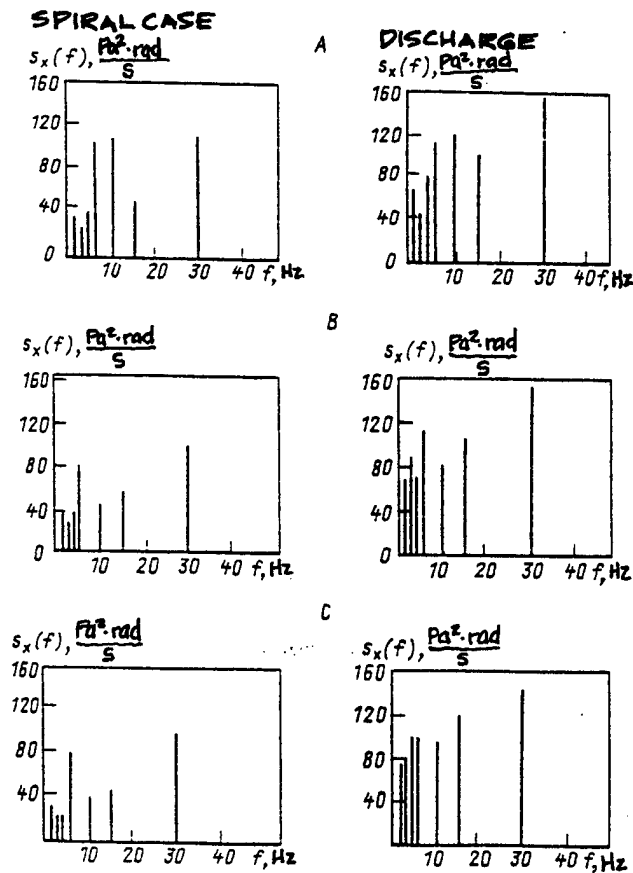
Fig. 3 shows the spectral characteristics of pressure pulsations in transits of the spiral case near the teeth and at the discharge branch.

The power of pressure pulsations in the middle part of the spiral case and in its discharge section differ significantly from each other. These differences are especially noticeable in $Q = 2.47$ m^3/s regimes where the pressure pulsation power at the discharge is double or more that in the middle sections. As the flowrate increases this difference decreases. At flowrates of $Q = 2.47$ m^3/s most of the pressure pulsation power increase occurs at frequencies of 2 and 2.5 Hz, i.e. in the low-frequency region where the process may be classified as random. As the flowrate itself increases a rise in hydrodynamic load is registered at the determined frequencies of f_{rot} and $2f_{rot}$; the maximum contribution occurs at $f = 2f_{rot}$. The spectrum of pressure pulsations on a discharge test bench and the spectrum of pump housing and drive motor support structure vibrations are roughly similar; this indicates that

Figure 3. Pressure Pulsation Spectra at the Pump Discharge in A, B and C regimes

the main reason for the increase in pump vibrations may be the hydrodynamic load occasioned by the change in pump operating regimes, in which the regime point on the characteristic curve approaches the boundary of the performance range. This in turn is occasioned by a change in the operating regime of the hydraulic network that includes the given pump.

The data obtained from this investigation allows us to verify the performance range of a pump when installing it and hooking it into the network, when the dynamic load at the performance boundaries needs to be determined[3]. It is a good idea to determine the coupling between pressure pulsations in flow sections of the pump set and vibration in the equipment outside the performance boundaries, as well as to find those frequencies at which dangerous increases in vibrations can arise. It is clear that this work should be carried out at the design stage of a PWSS and during startup testing of the pumps.

One of the most important network parameters is flowrate. A precise determination of flowrate for a comparatively mildly-sloping characteristic curve is one of the necessary conditions for finding the actual performance boundaries on the characteristic curve. Since the hard part in precisely determining the location of the regime point on a mildly-sloping characteristic curve is a precise determination of the flowrate, and at present this task is fraught with difficulties owing to the lack of reliable and accurate means of measurement, we suggest measuring the performance range from the amount of hydrodynamic load acting in the flow sections of a pump. For this purpose, in the course of pre-startup testing, control measurements of the dynamic loads in various operating regimes should be made, i.e. for various locations of the regime point on the characteristic curve. For the most reliable results when there are no reliable means of measuring the flowrate for the operating regime of a pump set, the current draw of the electric motor drive needs to be monitored.

Conclusions

1. In calculating and designing a hydraulic network for the process water supply system of an AES we need to account for the hydrodynamic loads arising in the flow sections of pump sets upon variation in the operating regimes of the consumers.

2. When centrifugal pump sets operate in a PWSS, the location of the regime point on the pump characteristic curve needs to be monitored. Excursions of the regime point beyond performance limits lead to significant increases in dynamic load: pressure pulsations and vibration.

3. The primary reason for increased vibration of pump sets is the effect of hydrodynamic pressure pulsations caused by the regime point going beyond performance limits. The frequency spectra of pressure pulsations and vibrations for the primary assemblies of a pump set are for the most part identical. As the flowrate increases an increase in the level of dynamic load at the rotation frequency and multiples thereof is noted. As the flowrate decreases there is an increase in the dynamic load registered at low-frequencies in the range from 2 to 4 Hz.

Bibliography

0. Margulova T.Kh. "Atomnyye electricheskiye stanstii" [Nuclear Power Plants], Moscow, Vysshaya shkola, 1984

0. Budov V.M. "Nasosy AES" [AES Pumps], Moscow, Energoatomizdat, 1986

0. Vissarionov V.I., Belyayev S.G. "A method for determining the dynamic load acting on the units of a pumping station" ENERGETICHESKOYE STROITELSTVO No 8, 1987

Characteristics of Idle Running of Turbine Stages and Sections

[Article by G. A. Shapiro, A. D. Kachan, and Ye. I. Efros, Kirov Polytechnic Institute and Belorussian Polytechnic Institute; first paragraph is verbatim IZVESTIYA AKADEMII NAUK BSSR SERIYA FIZIKO-ENERGETICHESKIKH NAUK English abstract]

[Text] The experimental results obtained have been employed to derive generalized relations for evaluation of the volume vapor flow rate and thermal gradient of turbine stages and sections with different geometric characteristics under zero efficiency conditions.

Investigation of the low-flow modes of turbine stages is of great importance in increasing the reliability and efficiency of turbines operating at partial loads. Specifically, such modes are characteristic for the low-pressure section of direct heating turbine plants.

Other research[1-6] has shown that, under actual turbine operating conditions, the economy of both the individual turbine stage and section with a specified geometry virtually singularly determine (given different combinations of mass steam flow and backpressure) either the magnitude of the available heat differential H_0 or the volumetric flow of steam at the outlet G_{v2}. A reduction in G_{v2} (or in H_0) leads to a reduction in the relative internal efficiency η_{oi} (and the used heat differential H_i) and a transition of the stages from the range of active modes with $H_i > 0$ to the region of energy consumption with $H_i < 0$. The idle run, i.e., that mode where the integral value of the internal power of a stage (section) has a zero value, is thus one of the singular operating modes of a turbine stage or section. Corresponding to the idle run are specific values of the volumetric flow of steam $(G_{v2})_{x.x}$ and available heat differential $H_{ox.x}$ for each stage (section). Knowing the values of $(G_{v2})_{x.x}$ and $H_{ox.x}$ is of great interest. This is connected with the fact that the methodological principles of determining sections' capacities changes in the range of modes with positive and negative efficiencies. In the range where a group of stages has a positive power, their efficiency may be satisfactorily described by the relative magnitude of the reduced ratio of their velocities,[5,7] whereas when $\eta_{oi} < 0$, the stages' power requirement is determined primarily by the steam density.[4]

14

Figure 1 presents the dependencies of the relative used and available heat differentials (H_i/H_{iH} and H_o/H_{oH}), where the subscript "H" refers the the mode with the rated volumetric flow of steam $(Gv_2)_H$, from $\overline{Gv_2} = Gv_2/(Gv_2)_H$ for the low-pressure sections of T-50-130, PT-60-130, PT-135-130, and T-180-130 turbines during operation with open grid valves. The experimental characteristics have been obtained on the basis of results of full-scale research, the method of which has been examined in rather great detail elsewhere.[4,8] Figures 1 and 2 also present data from the All-Union Heat Engineering Institute imeni F. E. Dzerzhinskiy regarding the last states of K-300-240 turbines produced by the Kharkov Turbogenerator Plant imeni S. M. Kirov [KhGTZ] and Leningrad Metal Plant imeni 22nd CPSU Congress [LMZ].[2,3]
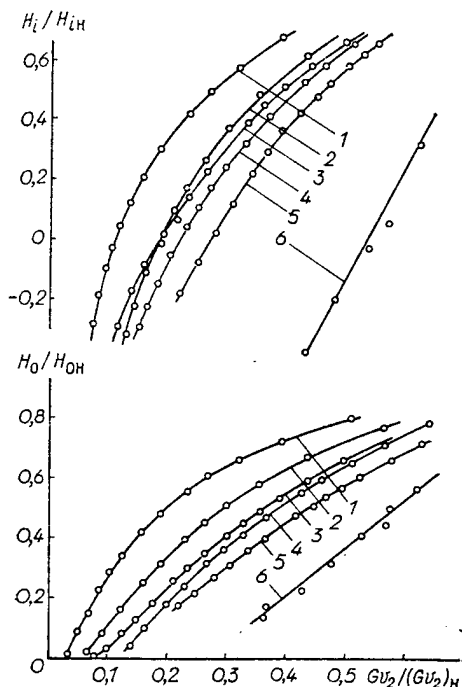
Figure 1. Dependence of the different turbine sections and stages used and the available heat differentials on the volumetric flow of steam: 1-4, low-pressure sections of PT-60-130, PT-135-130, T-50-130, and T-180-130 turbines; b, last stages of K-300-240 LMZ and K-300-240 KhGTZ turbines.
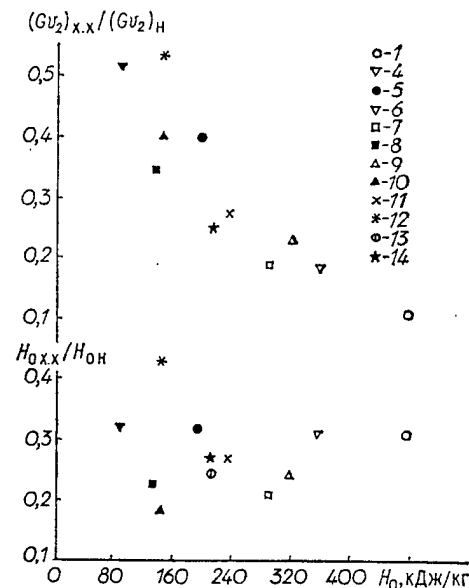
Figure 2. Magnitudes of the volumetric flow and available heat differential of the different states and sections in an idle run mode: 1, low-pressure section of a PT-60-130 turbine; 4 through 6, low-pressure section, the section consisting of stages 23-24, and stage 23 of a PT-135-130 turbine; 7 and 8, low-pressure section and stage 24 of a T-50-130 turbine; 9 and 10, low-pressure section (one flow) and stage 26 of a T-180-130 turbine; and 11 through 14, last stages of K-300-240 LMZ, K-300-240 KhGTZ, and K-100-90 turbines before and after updating.

The quantity $(\overline{Gv_2})_{x.x}$ (Figure 1) has very different values for different flow areas (the same applies to $\overline{H}_{ox.x}$). The magnitude of the available heat differential in the rated mode H_{oH} (Figure 2) has a significant effect on $(Gv_2)_{x.x}$; however, there is no singular correspondence between $(\overline{Gv_2})_{x.x}$ and

Hoн (or between $\overline{H}_{0x.x}$ and Hoн). Figure 2 presents additional data regarding the individual sections and stages of the low-pressure sections of the turbines under investigation. These data have been obtained by using power characteristics based on the method presented elsewhere.[4] In addition, extrapolation of the results of research conducted at the All-Union Heat Engineering Institute imeni F. E. Dzerzhinskiy[1] resulted in data regarding the idle run of the last stage of a K-100-90 turbine before and after updating.

To select the possible criterion possessing the idle run characteristics of different stages, we will, as a first approximation, examine a one-dimensional model of the steam flow under the hypothesis that the flow channels of the fixed and working blades are completely filled by the flow. For the specified conditions, in accordance with Euler's equation, the zero power of a state will occur when the peripheral components of the absolute flow velocity before and after the impeller are in equilibrium, i.e., when

(1)
$$c_1 \cos \alpha_1 = u - w_2 \cos \beta_2,$$

where c_1 and α_1 are the absolute velocity and angle at which the flow exits the guide apparatus, w_2 and β_2 are the relative velocity and angle at which the flow exits the rotating blade row, and u is the peripheral velocity of the impeller at its average diameter.

Considering that $c_1 = Gv_1/F_c$ and $w_2 = Gv_2/F_1$ (G being the mass flow rate of steam, F_c and F_1 being the outlet area of the channels of the nozzles and moving blades, and v_1 and v_2 being the specific volume before and after the rotating blade row), we obtain the following from (1):

(2)
$$\frac{(Gv_2)_{x.x} \cos \beta_2}{F_\pi u} = \frac{F_c/F_\pi}{\left(\dfrac{v_1}{v_2}\right)_{x.x} \dfrac{\cos \alpha_1}{\cos \beta_2} + \dfrac{F_c}{F_\pi}} .$$

In view of the sharply reduced heat differential in the idle run mode, the ratio $(v_1/v_2)_{x.x}$ included in (2) is little different from unity and has close values for the different stages. The same may be said regarding the magnitude of the ratio $\cos \alpha_1/\cos \beta_2$. For example, for the stages of the sections whose research results have been presented above, $\cos \alpha_1/\cos \beta_2$ is between 1.01 and 1.12. The decisive effect of the ratio of the outlet areas F_c/F_1 on the magnitude of the complex $(Gv_2)_{x.x} \cos \beta_2/(F_1 u)$ thus follows from (2). It should be noted that the quantity $F_1 u/\cos \beta_2$ is the volumetric flow of steam behind the stage in a mode with axial output of steam from the rotating blade row.

In a first approximation, a stage's available heat differential may be specified as

$$H_0 \approx \frac{w_2^2}{2\eta^*}\left(1 - \frac{w_1^2}{w_2^2} + \frac{c_1^2}{w_2^2}\right),$$

where η^* is the maximum relative internal efficiency when using the output velocity.

16

In an idle run mode, allowing for (1), we obtain

$$H_{0\,xx} \approx \frac{u^2}{2\eta^*} \frac{\left(1 - \frac{w_1^2}{w_2^2} + \frac{c_1^2}{w_2^2}\right)}{\left(\frac{c_1}{w_2}\cos\alpha_1 + \cos\beta_2\right)^2}$$

or (3)

$$\frac{u^2}{2H_{0\,x.x}\eta^*} \approx \frac{\left[\left(\frac{v_1}{v_2}\right)_{x.x}\cos\alpha_1 + \frac{F_c}{F_\pi}\cos\beta_2\right]^2}{\frac{F_c^2}{F_\pi^2}\left(1 - \frac{w_1^2}{w_2^2}\right) + \left(\frac{v_1}{v_2}\right)_{x.x}^2}.$$

Analyzing expressions (3) makes it possible to hypothesize that, just like the relative volumetric flow $(Gv_2)_{x.x}\cos\beta_2/(F_1 u)$, the characteristic ratio $u^2/(2H_{0x.x}\eta^*)$ depends primarily on F_c/F_1. In the case where the turbine stages have variable operating modes, the available heat differential is virtually singularly determined by the quantity Gv_2. This gives additional basis for using the general criterion to generalize data regarding $(Gv_2)_{x.x}$ and $H_{0x.x}$. The quantity η^* specifies the energy losses when steam flows in the channels of the cascade and characterizes the aerodynamic perfection of the flow area. Proceeding from this, the efficiency η^* is identified as an independent parameter of the stage. The resultant conclusions apply to individual stages. It was proposed that the following mean values be used for a section of turbine stages:

$$\tilde{u} = \sqrt{\frac{\Sigma u^2}{n}}\,; \quad \tilde{F}_\pi = \frac{\Sigma F_\pi}{n}\,; \quad \tilde{F}_c = \frac{\Sigma F_c}{n}\,; \quad \tilde{\beta}_2 = \frac{\Sigma\beta_2}{n}\,,$$

where n is the number of stages in the section. The angle β_2 is specified as $\beta_2 = \arcsin(F_1/F_T)$, where F_T is the face area of the impeller.

Considering what was said above, the research results (Figure 3) were processed accordingly. The experimental data regarding both individual stages and sections of different turbines (Figure 3) are satisfactorily generalized by the dependencies

$$\frac{(Gv_2)_{x.x}\cos\tilde{\beta}_2}{\tilde{F}_\pi\tilde{u}} = f\left(\frac{\tilde{F}_c}{\tilde{F}_\pi}\right)\,; \quad \Sigma u^2/(2H_{0\,x.x}\eta^*) = \varphi\left(\frac{\tilde{F}_c}{\tilde{F}_\pi}\right).$$

The good agreement of the data with respect to $(Gv_2)_{x.x}$ of the model stages with a high degree of fanning[9] and from a full-scale experiment should also be noted.

The dependencies presented in Figure 3 may be approximated with sufficient precision (the broken lines) by the functions

(4)
$$(Gv_2)_{x.x}\cos\tilde{\beta}_2/(\tilde{F}_\pi\tilde{u}) \approx a\tilde{F}_c/\tilde{F}_\pi,$$

(5)
$$\Sigma u^2/(2H_{0\,x.x}\eta^*) \approx b\tilde{F}_c/\tilde{F}_\pi,$$

17

where the coefficients are as follows: a = 0.64 and b = 2.28.

Figure 3.   Effect of the ratio of the outlet areas of the nozzle and rotating blade row on the idle run characteristics of the following sections and stages: 1 through 3, the low-pressure section, sections consisting of stages 27 through 29 and 27 through 28 of a PT-60-130 turbine; 4 through 6, the low-pressure section, the section consisting of stages 23 and 24, and stage 23 of a PT-135-130 turbine; 7 and 8, low-pressure section and stage 24 of a T-50-130; 9 and 10, low-pressure section (one flow) and stage 26 of a T-180-130 turbine; 11 through 14, last stages of K-300-240 LMZ, K-300-240 KhGTZ, and K-100-90 turbines before and after updating; 15, model stages[9]; and 16, an approximation.
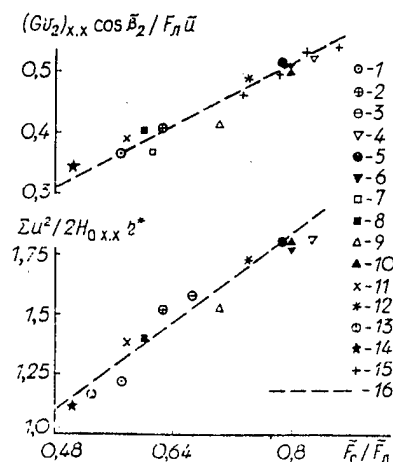
In accordance with (4) and (5), the idle run mode of a stage or section occurs when the volumetric flow of steam is reduced to the value

$$(Gv_2)_{x.x} \approx a\tilde{u}\tilde{F}_c/\cos\tilde{\beta}_2;$$

in which case the available heat differential amounts to

$$H_{0\,x.\,x} \approx \tilde{F}_{\pi}\Sigma u^2/(2b\tilde{F}_c\eta^*).$$

The relative means square error in approximating the experimental data by functions (4) and (5) is at a level of 4 percent, which is commensurate with the error of the experiment.   Considering this and bearing in mind the rather broad range of geometric characteristics of the stages studied, it is possible to recommend dependencies (4) and (5) for estimating the idle run parameters of different turbine stages and sections.

Conclusions

1.   It was discovered from an analysis of the physical processes in a turbine stage and confirmed experimentally that the ratio of the minimum areas of the nozzle channels and rotating blade row $\tilde{F}_c/\tilde{F}_{\pi}$ is a convenient design parameter for generalizing the idle run characteristics of turbine stages and sections.

2.   Generalized dependencies have been derived that make it possible to determine the volumetric flow of steam $(Gv_2)_{x.x}$ and the available heat differential $H_{0x.x}$ in a mode with zero efficiency for turbine stages and sections with different design characteristics.

Bibliography

1.   Lagun, V. P., and Simoyu, L. L., TEPLOENERGETIKA, No 8, 1969, pp 13-17.

2. Lagun, V. P., et al., "Kotelnyye i turbinnyye ustanovki energeticheskikh blokov: Opyt osvoyeniya" [Boiler and Turbine Power-Generating Units: Experience of Placement Into Operation], ed. by V. Ye. Doroshchuk, Moscow, 1971, pp 157-171.

3. Lagun, V. P., Simoyu, L. L., Nakhman, Yu. V., and Pakhomov, V. A., TEPLOENERGETIKA, No 4, 1984, pp 26-32.

4. Shapiro, G. A., "Povysheniye effektivnosti raboty TETs" [Increasing Operating Efficiency of TETs], Moscow, 1981, 200 pages.

5. Kachan, A. D., "Rezhimy raboty i ekspluatatsii teplovykh elektricheskikh stantsiy" [Operating Modes and Performance of Electric Power Plants], Minsk, 1987, 318 pages.

6. Benenson, Ye. I., ENERGOMASHINOSTROYENIYE, No 12, 1960, pp 33-36.

7. Samoylovich, G. S., and Troyanovskiy, B. M., "Peremennyye i perekhodnyye rezhimy v parovykh turbinakh" [Variable and Transient Modes in Steam Turbines], Moscow, 1982, 496 pages.

8. Inventor's certificate 570802 (USSR), BYUL. IZOBRET., No 32, 1977.

9. Shnee, Y. I., Ponomarev, V. N., and Bystritskiy, L. N., ENERGOMASHINOSTROYENIYE, No 11, 1977, pp 10-14.

UDC 535.211

Model of Laser Heating of Metal in Liquid Medium and Its Approximate
Approbation

[Article by V. D. Dzhunushaliyev and E. X. Chokoyev, Physics Institute, AN
Kirghiz SSR, and Kirghiz State University imeni 50th Anniversary of the USSR]

[Text] Laser technology is becoming increasingly important in modern methods
of treating materials. This is precisely why a great deal of attention is
being paid to basic and applied research on this, particularly to methods of
laser hardening a metal surface. The majority of works in this direction
relate to laser treatment in gaseous media, although the idea of the
possibility of laser hardening in liquid media has recently been expressed.[1]
Because of their great heat release, the cooling processes in these media
occur much more intensively than in a gaseous medium. Treating the surface of
a steel product in a liquid medium by using a moving laser beam increases the
hardness of its surface significantly.

The nature of the occurrence of thermophysical processes in metal when it is
treated in a liquid medium by a moving laser beam may be explained by solving
the following heat conduction equation:

$$(1) \qquad c\rho \, \frac{\partial T(x,y,z,t)}{\partial t} = \lambda \, \Delta \, T(x,y,z,t)$$

here c, ρ, and λ are respectively the heat capacity, density, and temperature
conduction coefficient of the material, and T is its temperature. The
equation ignores the dependence of the temperature conduction coefficient on
temperature. Let the coordinate plane XY lie on the surface of the specimen
and the OZ axis be perpendicular to this surface. To simplify the problem, we
will examine a rectangular plate. The boundary conditions have the following
form:

$$(2) \qquad \lambda \, \frac{\partial T}{\partial z}\bigg|_{z=0} = q_0 exp\left\{-\left[\left(\frac{x_0-V_x t}{\sigma}\right)^2 + \left(\frac{y_0-V_y t}{\sigma}\right)^2\right]\right\} + q$$

here the first term in the right part describes the heating of the plate by a
laser beam, q_0 is the intensity of the laser radiation at the center of the

irradiated spot, x_0 and y_0 are the coordinates of the initial point of the beam's motion, σ is the characteristic size of the beam, V_x and V_y are projections of the velocity vector of the laser beam's motion in the plane XY, and the second term describes the cooling of the heated plate in the surrounding space through its upper surface.

$$(3) \qquad \lambda \frac{\partial T}{\partial z}\bigg|_{z=h} = q$$

$$(4) \qquad \lambda \frac{\partial T}{\partial u}\bigg|_{s} = q$$

Boundary conditions (3) and (4) describe heat release to the surrounding space through the plate's lower and side surfaces, respectively. We will further assume that the liquid medium is water.

It should be noted that cooling in water at high temperatures is essentially nonlinear.[2,3] This is related to the fact that the following modes of heat release into water are observed as a function of T:

1. Convective heat transfer

$$(5) \qquad q = q_{conv} = -\alpha_{conv}(T - T_0); \quad T \leq T_1$$

here q_{conv} is the coefficient of convective heat transfer, and T_0 is the temperature of the environment.

2. Nucleate boiling

$$(6) \qquad q = q_{nucl} = -[\beta(T - T_s)]^n; \quad T_1 \leq T \leq T_2$$

T_s is the temperature of the boiling liquid, and β and n are empirical coefficients.[2]

3. Film-type boiling

$$(7) \qquad q = q_{film} = -\alpha_{film}(T - T_s); \quad T \geq T_s$$

α_{film} is the coefficient of heat release in the case of film-type boiling.

4. An intermediate mode in which $T_2 \leq T \leq T_3$. The dependence $q(T)$ in this case is determined by the condition of the joining of the modes of film-type and nucleate boiling.

We determined the temperatures T_1, T_2, and T_3 at which the change in cooling modes occurs from the experimental dependence of the heat flow on the temperature of the body's surface[3] (see Figure 1). As is evident, linear heat conduction equation (1) with the nonlinear boundary conditions (2) through (7) is practically impossible to solve analytically. Even solving it numerically in full measure is a very complicated task. Therefore, to test the model in a first approximation, we reduced the three-dimensional non-steady-state heat

21

conduction equation (1) to a one-dimensional non-steady-state equation. Physically, this means that the heating of a thin rod by a moving laser beam was examined.

Figure 1. Piecewise-linear approximation of heat release by a heated surface into a liquid medium.

In view of the fact that the rod was considered infinitely thin, the processes of both the arrival of the heat and the cooling were described by including the heat sources in the heat conduction equation:

$$(8) \qquad c\rho \frac{\partial T}{\partial t} = \lambda \frac{\partial^2 T}{\partial x^2} + q_v$$

here q_v is the right part of boundary condition (2). Heat transfer with the environment in accordance with one of the modes (3) through (7) was specified at the ends of the rod depending on their temperature.

The numerical solution was performed by the sweep method in accordance with a scheme described elsewhere.[4] Its analysis showed that, in a time on the order of several seconds, the heat transfer process stabilizes and movement of the hot spot (which remains practically unchanged in shape) behind the laser beam is observed (Figure 2).
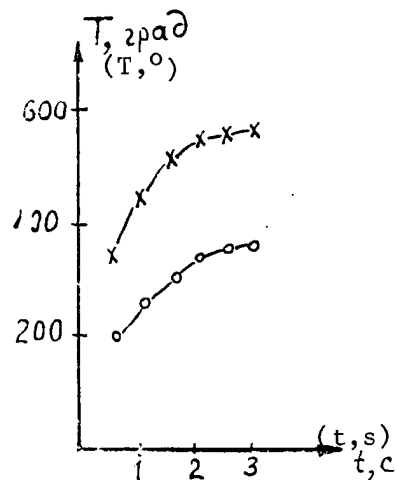

Figure 2. Change in the maximum temperature in the center of a hot spot over time.
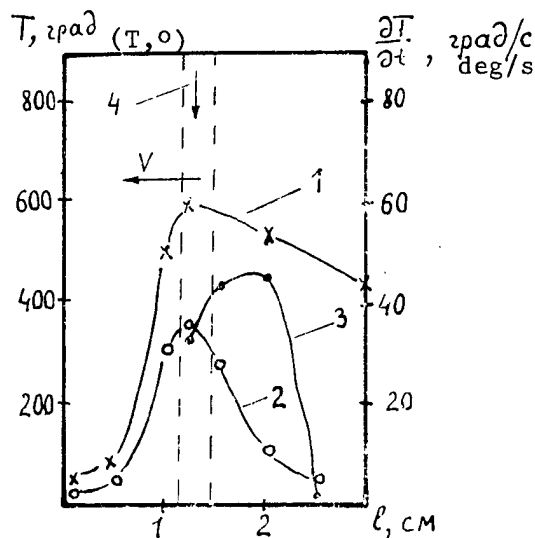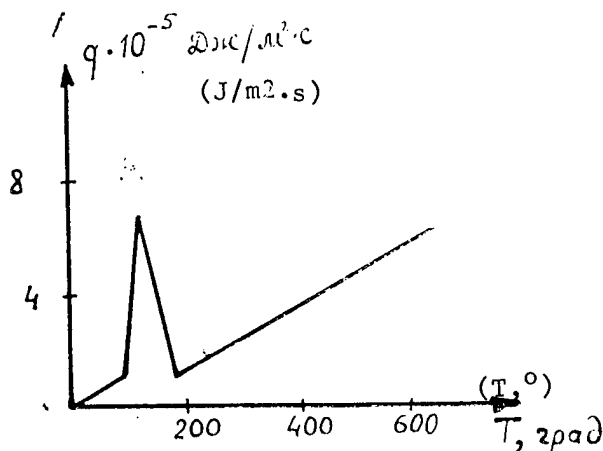
Figure 3. Temperature profiles (1, 2). Ratio of the speed of cooling in water to the speed of cooling in air (3); 4, indicates a laser beam.

Figure 3 presents the characteristic temperature distributions that move at the constant rate V. Curves 1 and 2 describe the heating and cooling in air

22

and in water, respectively, given the following parameters: laser beam power, Q = 1kW; beam velocity, V = 1 cm/s. It is evident that under the effect of a moving laser beam, the rate of cooling in a liquid medium is approximately two orders of magnitude greater than the rate of cooling in air.

The calculations showed that in the rate interval investigated by us from 0.1 to 1.0 cm/s and with a laser beam diameter of 0.5 to 2.0 mm, the size of the hot spot (defined as the region in which the temperature exceeded half the maximum value of the temperature) depends, for practical purposes, solely on the power of the laser radiation.

It is evident from an analysis of the solution to the equation for heat conduction at different speeds, laser radiation powers, and cooling capabilities on the part of the environment that the existing asymmetry of the instantaneous temperature distribution in the rod is strongly dependent on the cooling capability and, to a lesser degree, dependent on the remaining parameters. We will also note that the problem of the heating and cooling of a specimen hardened by a moving energy source has already been examined.[5-7] These solutions do not, however, consider cooling, nonlinearity in the boundary conditions, and limited dimensions of the heated body.

In conclusion, the authors express their gratitude to Zh. Zh. Zheyenbayev, corresponding member of the Kirghiz SSR Academy of Sciences, for his useful discussions.

Bibliography

1. GDR Patent No 217738 A1, 1985.

2. Kobasko, N. I., "Zakalka stali v zhidkikh sredakh pod davleniyem" [Hardening Steel in Liquid Media Under Pressure], Kiev, Naukova Dumka, 1980.

3. Kutateladze, S. S., and Borishanskiy, V. M., "Spravochnik po teploperedache" [Manual on Heat Transfer], Moscow, Gosenergoizdat, 1959.

4. Kozdoba, L. A., "Metody resheniya nelineynykh zadach tepolprovodnosti" [Methods of Solving Nonlinear Heat Conduction Problems], Moscow, Nauka, 1975.

5. Ustinov, N. G., "Using Asymptotic Laplace Method To Calculate Temperature Fields From Moving Concentrated Sources," FIZ. I KHIM. OBRABOTKI MATERIALOV, No 1, 1985, pp 26-35.

6. Kolyano, Yu. M., Kokora, A. N., Bernar, I. I., Tetushkin, S. P., and Makhorkin, I. N., "Temperature Fields in Components of Cotton-Cleaning Equipment During Continuous Laser Treatment," FIZ. I KHIM. OBRABOTKI MATERIALOV, No 1, 1985, pp 33-42.

7. Rykalin, N. N., Uglov, A. A., and Smurov, I. Yu., "Three-Dimensional Nonlinear Problems of Heating Metals by Laser Radiation," FIZ. I KHIM. OBRABOTKI MATERIALOV, 1979, pp 3-13.

UDC 528.5

New Mock-Up of DVSD-1200 Light Range Finder and Test Results

[Article by R. A. Movsesyan, K. S. Gyunashyan, Ye. A., Ayrapetyan, and G. A. Babayan, Yerevan State University, under the "Measuring Technology" rubric: "New Mock-Up of DVSD-1200 Light Range Finder and Test Results"; first two paragraphs are IZVESTIYA AKADEMII NAUK ARMYANSKOY SSR: SERIYA TEKHNICHESKIKH NAUK abstract]

[Text] This article describes the development and recommendation of a new mock-up of the DVSD-1200 light range finder that includes the principal advantages of a microwave light range finder under conditions of strong perturbing effects: sharp temperature differentials, atmospheric turbulence, air pollution, etc. Thanks to the introduction of an electronic counter, the time required to make measurements was reduced by a factor of five, which makes it possible to increase the number of measurements and reduce the random error in making the final measurement of the phase cycle.

Laboratory and industrial tests of the mock-up on comparators at the Yerevan Physics Institute, the Institute of High-Energy Physics, and in the network of the USSR Academy of Sciences' Institute of Nuclear Research ranging network showed the reliability and high-precision of the mock-up's measurement. Figures 3, references 4.

Among research on the key parameters and shortcomings of mock-ups of DVSD-1200 light range finders, two works[1,2] contain the most complete information. As a result of the research conducted, these works reveal a number of significant flaws in the mock-ups: the limitation of the temperature range of the light range finder's operation; the error in the readout device making the final measurement of the phase cycle; and the inadequate stability of the microwave oscillator's frequency, without the removal of which the production of DVSD-1200 instruments will not be feasible.[3]

Figure 1 is a block diagram of the new mock-up of the DVSD-1200 light range finder. The plane-polarized laser beam (1) of a type LGN-207 A laser is directed by mirrors (2) to a light modulator (3) on a KDR [not further identified] crystal mounted on a cylindrical cavity with a central conductor
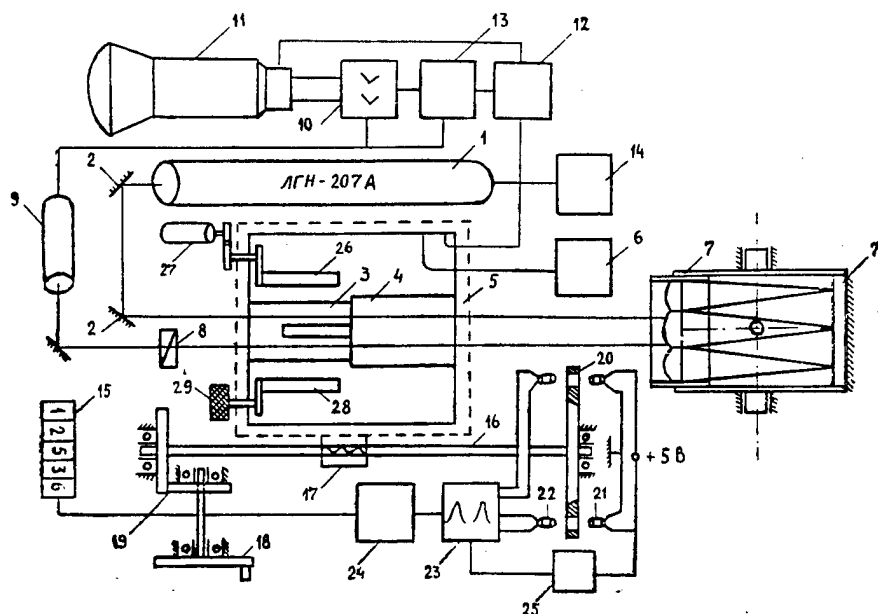
Figure 1.

(4). The cavity is mounted on a positioning table (5) mounted on guides to move the light modulator 140 to 150 mm along the path of the beam's passage. A type E_{01} wave is excited by a microwave oscillator in the light modulator's cavity. The modulated beam is directed to a mirror-and-lens reflector consisting of movable objects (7) and a fixed mirror (7') with a diameter of 90 mm. A groove on the crystal from the side of the maximum intensity of the cavity's electrical field reduces the modulator's losses and prevents rays reflected from the crystal's outlet face in the transmission channel from falling onto the photoreceiver (9) that is mounted after the analyzer (8). Depending on the position occupied by the light modulator, light with an intensity of I_M arrives at the type FEU-68 photoreceiver. Its amplitude depends on the magnitude of the voltage U on the crystal and the intensity of the receiving beam I^4

(1)
$$I_M = 0{,}5I\{1 - I_0\left[2\pi U/U_\pi \cos\left(2\pi D/\lambda_M\right)\right]\},$$

where I_0 is a zero-order Bessel function and U_π is the voltage that must be applied to the crystal to turn the polarization $90°$.

The effectiveness of increasing the power lies in the fact that there is a remodulation of the light, the maxima of the intensity of the light expand or double, and in the region of the minima of the light there is an increase in the curvature of the demodulation curves, which are shown in Figure 2. The designation "indication level" in Figure 2 refers to the minimum ratio I_m/I conditioning the differentiating signal on the light range finder's indicator. The experimentally determined "indication level" for the new mock-up amounted to $I_m/I = 1.2 \cdot 10^{-4}$. The following equality takes place for all points D' at the indication level according to which the position of the light's minimum is determined:

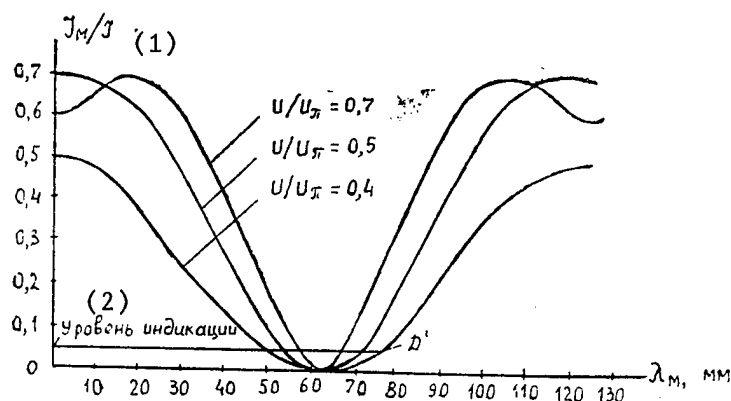$$1{,}2 \cdot 10^{-4} = 0{,}5\{1 - I_0\{2\pi U/U_\pi \cos\left(2\pi D'/\lambda_M\right)\}\},$$

25

from where

$$D' = \frac{\lambda_{_M}}{2\pi} \arccos \frac{49 \cdot 10^{-4}}{U/U_\pi} .$$

Figure 2.

Key:

1. I_m/I
2. Indication level

To determine the degree of the effect that the quantities included in expression (2) have on the curvature of the demodulation curves when the indication level is specified as $I_m/I = 1.2 \cdot 10^{-4}$, it is best to differentiate expression (1) with respect to D':

$$\frac{dI_{_M}/I}{dD'} = -\frac{2\pi^2}{\lambda_{_M}} \cdot \frac{U}{U_\pi} \sin \left(\frac{2\pi D'}{\lambda_{_M}} \right) I_0 \left(2\pi \frac{U}{U_\pi} \cos \frac{2\pi D'}{\lambda_{_M}} \right) .$$

(3)

Calculations based on expression (3) at different intensities of receiving light I and different ratios U/U_π showed that, when the magnitude of I changes by a factor of n, the curvature changes by a factor of $n^{0.5}$. In addition, an increase in the light's intensity does not always lead to an increase in the measurement precision. The characteristics of the multiplier phototube show that, to increase the curvature of the curves in Figure 2, the indication level should be at the level of the light's weak intensity. The pulses from the multiplier phototube's outlet are fed to an amplifier (10), amplified with respect to amplitude, and fed to the signal plates of a type 6L01I small tube (11).

Pulses from the light modulator that are amplified in the form of saw-toothed pulses are used for simultaneous scanning and synchronization of the pulses observed on the tube's screen, and the scanning pulses from the shaper's outlet (12) are fed to the tube (11). In this case the scanning amplitude on the tube screen shows the resonance tuning of the light modulator.

Figure 3 shows indication signals that are characteristic for the following operating conditions: a) the receiving beam has no fluctuations or polarization irregularities, and there are no harmonics in the modulation frequency; b) the receiving beam has a polarization irregularity and fluctuations, and there are no weak amplitude harmonics in the frequency; c) the receiving beam is normal, and there are weak amplitude harmonics in the frequency; and d) the amplitude of the harmonics is large, and there is an irregularity in the receiving beam.

Figure 3.

Key:

1. Modulation pulse
2. From the harmonics

(1) импульс модуляции

(2) от гармоник

a. a   б. b   в. c   г. d
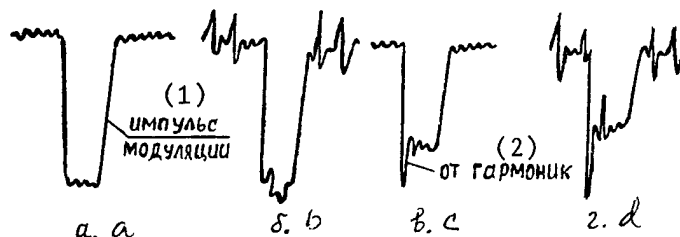
Pulses a and b in Figure 3 took place when the modulator was powered by a lamp generator with an output power of P = 100 W without a isolation gate between the modulator and generator. Pulses c and d were obtained with a transistor generator with an isolation gate (P = 150 W). The presence of harmonics in / the modulation frequency reduces the efficiency of light modulation and results in the presence of residual light.

Two wafers of KDR crystal were introduced into the modulator's cavity. One of the plates (26) was connected to an electric motor (27) and controlled from the instrument's front panel, while the other plate (28) was connected to a handle (29) located inside the instrument. Both plates turn around their axes and change the modulator's resonance frequency. The handle (29) is frequently set in stages depending on the temperature of the medium, while the electric motor is set continuously as a function of the magnitude of the crystal's heating during the process of the instrument's operation.

The mock-up of the new light range finder is made in two versions. In one, the receiver-transmitter has less of a slope (12 to 14°); in the other, it has more of a slope (50 to 60°). The first mock-up is intended for operation at a fixed frequency in a DVSD [not further identified] mode, whereas the second is intended for operation in a VSD [not further identified] mode with a grid of scale frequencies. The basis of both oscillators is a GIATsINT commercial thermostatted quartz master oscillator operating at a frequency of 5 MHz.

The set-up for moving the light modulator and the device indicating the final measurement of the phase cycle have been changed in the new mock-ups of the light range finder. A high-precision screw (16) with a pitch of 4 mm that is fixed between two supports is used for this. The screw (16) is connected with the light modulator's table (5) through a nut (17) made of fluoroplastic. A friction coupling (19) is used to protect the movement limiters from external forces applied to the handle (18) that turns the screw (16). To operate the counter (15), a disk (20) with jaws having a spacing of 0.5 to 0.6 mm is mounted at the other end of the screw. The counting pulses are shaped when light passes from light-emitting diodes (21) through a slit in the disk (20) to photodiodes (22). An electronic pulse multiplier (23) is used to shape 400 pulses in one turn of the disk (20). The modulator's position is determined with an error of 0.01 mm. In the pulse summer, 24 pulses are summed as the modulator moves to one side and are removed when it changes direction. In addition, each reading of the position of the minimum of the receiving signal is written, and the mean value is output to the counter's (15) display screen. Each reading may be obtained by an instruction from the observer.

The counter (15) is a five-digit digital display in which the final measurement of the phase cycle in millimeters is illuminated, for example,

125.36. Thanks to the introduction of an electronic counter and readout summer, the time required to make measurements is reduced by about a factor of 5, while one series of measurements from five binary receivers takes 30 seconds.

From a design standpoint, the new mock-up consists of three units: a receiver-transmitter, a microwave oscillator, and a reflector. The receiver-transmitter is designed and constructed on the basis of separate power supply circuits (13), (14), and (25). The small unit to supply power to the laser (14) is mounted on the receiver-transmitter. The tube (11), photoreceiver (9), and amplifier and scanner circuits are powered from one source (13), while the entire counter has its own stabilized power supply (25). The receiver-transmitter's power requirement amounts to a total of 17 W, 10 W of which is used by the laser. The transistor-based microwave oscillator uses 18 W, 8 W of which are used by the quartz oscillator's thermostat.

Laboratory and industrial tests of the mock-up on comparators at the Yerevan Physics Institute, the Institute of High-Energy Physics, and the ranging network of the USSR Academy of Sciences' Institute of Nuclear Research in 1986 showed that the mock-up operates reliably, that its optical units do not require alignment, and that its electrical circuits do not need tuning after it has been transported.

Bibliography

1. Vaynberg, V. Ya., and Shirov, F. V., "Studies of Mock-Ups of Type DVSD-1200 Light Range Finder With Mirror Collimating System," GEODEZIYA I KARTOGRAFIYA, No 4, 1983, pp 17-20.

2. Potthoff, H., "Untersuchunger am elektrooptischen Prarisions-Entferhungsmebgerat DVSD-1200," VERMESSUNGSTECHNIK, Vol 28, No 10, 1980, pp 325-328.

3. Movsesyan, R. A., et al., "DVSD-1200 High-Precision Electrooptic Light Range Finder," GEODEZIYA I KARTOGRAFIYA, No 9, 1973, pp 14-18.

4. "Ekspress-informatsiya 'Radiolokatsiya, televideniye, radiosvyaz'" [Express Information "Radar, Television, Radio Communications], No 24, 1966, pp 1-11.

Calculating Jaw Profile of Industrial Robot Wide-Range Centering Gripping Mechanism

[Article by F. B. Kim, candidate of technical sciences, and Gomes Nelson, student; first two paragraphs are IZVESTIYA VYSSHIKH UCHEBNYKH ZAVEDENIY: MASHINOSTROYENIYE abstract]

[Text] This article discusses a method for numerical calculation and design of the jaw profile of a wide-range gripping mechanism for an industrial robot. The method makes it possible to conduct profiling with any previously specified precision depending on the discreteness selected for specifying the component radius.

The rational significance of the initial parameter, i.e., the angle at the point of the "knife edge," is examined by proceeding from the principle that imprecision in manufacturing the profile has a minimum effect on the centering error.

Gripping mechanisms are among the most important components of industrial robots. They must possess high flexibility relative to the parameters of the manipulation object and, to the degree possible, must not complicate programming of the industrial robot. This is achieved by the positional invariance of the manipulation objects to their parameters in the coordinate system connected with the manipulator's last link. For bodies of revolution this condition is met by using quick-change or wide-range centering gripping mechanisms, the most compact designs of which are connected with the use of turning jaws with a special profile.

RTM 2 R00-1-78 stipulates a method for the approximate design of a jaw profile along the arcs of a circle.[1] The centering error (maximum deviation of the component's axis from its nominal position) is determined by the dependence

$$\delta = \pm \frac{(D_{max} - D_{min})^t}{4096 R^3} \, \mathrm{tg}^2\beta,$$

(1)

where D_{max} and D_{min} are the component's maximum and minimum diameter; R is the distance between the jaw's turn axis and the component's axis; and β is half

the angle of the "knife edge," i.e., the angle between the tangent to the component at the jaw's contact points (Figure 1). It will be shown below that $\beta = \beta_1 = \beta_2$. Analysis of 1 shows that the centering error is small when the changes in the components' diameters are small. However, when $D_{max} = 160$ mm, $D_{min} = 0$, $R = 130$ mm, and $\beta = 55°$, the centering error δ amounts to ± 0.149 mm. Given the modern requirements that the error in positioning industrial robots' end-effectors be on the order of ± 0.1 mm or less, such an error may be inadmissible. It is therefore advisable to develop a method of calculating and constructing a more exact profile for centering turning jaws given an expanded range of change of the components' diameters.

A method for numerical calculation and design of the profile of the centering turning jaws of wide-range gripping mechanisms is proposed.

The source data for calculation of the profile are as follows: β_1, half the angle at the point of the "knife edge"; r_{max}, the maximum radius of the component manipulated; and R, the distance between the jaw's turning axis and the component's axis (Figure 1). In accordance with the theorem of cosines, from an analysis of the triangle ABO

$$(2) \qquad \rho_1 = \sqrt{R^2 + r^2 - 2Rr\cos\beta_1},$$

where ρ_1 is the radius vector of the point B at which the upper side of the centering profile makes contact with the component and r is the component's radius.

The respective angular coordinate φ_1 must be calculated to fully specify the position of the point B in the polar coordinate system connected with the turning jaw, the initial axis X of which passes through the centering profile corresponding to a component with a zero radius.

It follows from Figure 1 that

$$(3) \qquad \varphi_1 = \alpha - \psi_1,$$

where

$$(4) \qquad \psi_1 = \arcsin(r\sin\beta_1/\rho_1),$$

α being the angular coordinate of the component relative to the OX axis.

Figure 1.

When the increment of the component's radius Δr (Figure 2) is small, it follows from the triangle A_1A_2D that $A_1A_2 = \Delta\alpha R$, the angle $DA_1A_2 = \beta_1$, and $DA_2 = \Delta r$. Consequently, $\Delta\alpha = \Delta r/R\sin\beta_1$, and when (5) is integrated with respect to r, we obtain
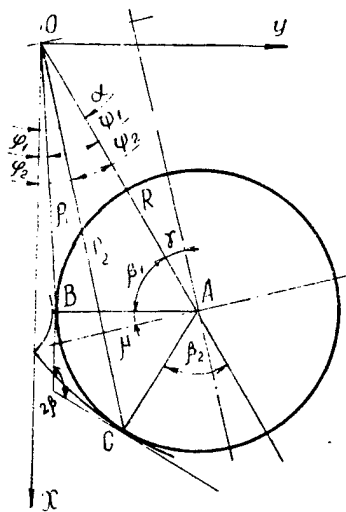
$$(5) \qquad \alpha = r/R\sin\beta_1.$$

30

By substituting (4) and (5) into (3) we obtain an expression for determining φ_1. In order to unequivocally determine the position of the component's axis relative to the gripping mechanism, besides the point B found on the upper side of the profile, we must also fine the respective point C on the lower side.

Since the angle β_2 (Figure 2) has not been previously specified, it follows from $\triangle A_1 A_2 E$ that $\angle A_2 A_1 E = \beta_2$. Then, by analogy with (5),

(6) $\qquad\qquad \beta_2 = \text{acrsin}\,(\Delta r / R\,\Delta\alpha),$

however, in accordance with (5), $\Delta\alpha = \Delta r\,\sin\beta_1$; consequently,

Figure 2.

$$\beta_2 = \arcsin\frac{R\,\Delta r\sin\beta_1}{R\,\Delta r} = \arcsin\beta_1 = \beta_1 = \beta.$$
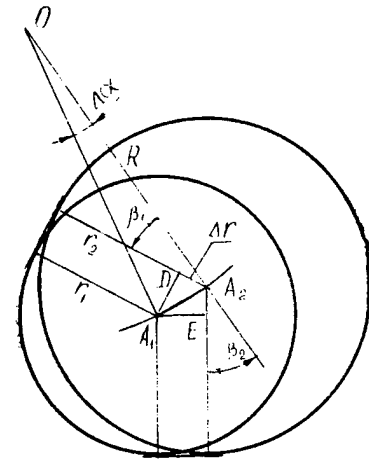
By analogy with (2) through (4), it is possible to specify the following:

(7) $\qquad\qquad \rho_2 = \sqrt{R^2 + r^2 + 2R\,r\cos\beta_2},$

(8) $\qquad\qquad \psi_2 = \arcsin\,(r\sin\beta_2 / \rho_2),$

(9) $\qquad\qquad \varphi_2 = \alpha - \psi_2.$

For convenience of use, the coordinates B and C may be transferred to a cartesian coordinate system:

$$x_B = \rho_1\cos\varphi_1, \quad x_C = \rho_2\cos\varphi_2,$$

(10) $\qquad\qquad y_B = \rho_1\sin\varphi_1, \quad y_C = \rho_2\sin\varphi_2.$

Analysis of the change in the coordinates of the points shows that, as the radius of the component r increases, there is initially a reduction ρ_1, and then, from that moment on, an increase. Profiling showed that a segment constructed when $\rho_{1(i)} \geq \rho_{1(i-1)}$ is subject to trimming. It follows from an analysis of (2) for the extreme that this phenomenon occurs when

(11) $\qquad\qquad r_{ext} = R\cos\beta_1,$

with

(11') $\qquad\qquad \rho_{1ext} = R\sin\beta_1.$

Consequently, r_{ext} is the maximum radius of the component at which a turning jaw profiled according to the method presented centers the component.

If the gripping mechanism's design parameters (for example, the distance to that element of the gripping mechanism that is nearest to the component's

31

axis) allows blank dimensions of more than r_{ext} and this capability must be used, the jaw profile may be adjusted further. All that is necessary is another profiling law under which all components with a radius greater than r_{ext} are tangent to the upper side of the profile at the point specified for $r = r_{ext}$, and the coordinates of the points on the lower side are specified in accordance with the method presented below.

It is assumed that $\rho_i{}^* = \rho_{1ext} = \text{const}$, $\phi_1{}^* = \phi_{1ext} = \text{const}$, $x_B{}^* = x_{Bext} = \text{const}$, and $y_B{}^* = y_{Bext} = \text{const}$.

The angular coordinate of the point A of the component's axis is determined in accordance with the expression

$$(12) \qquad \alpha_{(i)} = \alpha_{(i-1)} + \Delta\alpha,$$

where $\alpha_{(i)}$ is the value of α for the current computation cycle and $\alpha_{(i-1)}$ is the value for the previous cycle,

$$(13) \qquad \Delta\alpha = \psi_{1(i)} - \psi_{1(i-1)}.$$

The value $\psi_{1(i-1)}$ is determined from the preceding calculation cycle, and that of $\psi_{1(i)}$ is determined from the expression (Figure 1)

$$(14) \qquad \psi_{1(i)} = \arccos\left[(R^2 + \rho_1{}^{*2} - r^2)/2R\rho_1{}^*\right].$$

To determine β_2, it is necessary to find (on the basis of (6)) that value of β_2 that will not be constant under the new conditions. Next, the coordinates of the respective point of the lower side of the jaw's profile are determined in accordance with (7) through (9).

By performing calculations in accordance with the method presented, beginning with $r = 0$, it is possible to determine the jaw profile with any previously specified precision depending on the discreteness of the change in the component's radius that is selected. Jumping to the second profiling law is possible in accordance with (11) when the value of r_{ext} has been previously specified. A conditional jump when $\rho_1 \geq R \sin \beta_1$ may result in an error since $R \sin \beta_1 = \rho_{1min}$. An conditional jump when $\angle OBA \geq \pi/2$ is more reliable

$$(15) \qquad \beta_1 + \psi_1 \leqslant \pi/2.$$

The proposed method may easily be included in a simple program for calculating the jaw profile of a centering gripping mechanism on a computer.

The angle at the point of the "knife edge" has a significant effect on the shape of the jaw's profile, the amount the jaw opens, the torque applied to the jaws, the dependence of the centering error on the imprecision of the manufacture of the jaw profile, and the reliability of holding the component.

The condition of the reliability of holding the component entails having the arc distance between those points of contact between the gripping mechanism and component that are most remote from one another not exceed $180° - 2\mu$,

32

where μ is the friction angle. For a symmetrical gripping mechanism, this condition has the following form (Figure 1): $\beta_1 \le 59°$ to 69°.

From an analysis of the effect of β on the torque applied to the jaws, we obtain the following in a first approximation:

$$M_{кр} = (KGRf \sin \beta)/2,$$

where K is the safety factor, G is the weight of the blank, and f is the coefficient of the component's friction against the gripping mechanism's jaw. All these quantities, with the exception of β, may be considered constant. Consequently, when β is increased, the torque increases.

The effect of the size of the angle β on the dependence of the centering error on the imprecision of manufacturing the tooth profile Δ is broken down into two cases: the imprecision of manufacture Δ on one side of the jaw (δ_1) and the imprecision of manufacture Δ on both sides of the jaw (δ_2). It is not difficult to show that in the first case the centering error $\delta_1 = \Delta/\sin 2\beta$, whereas in the second case $\bar{\delta}_2 = \bar{\delta}_1 + \bar{\delta}_1'$ or $\delta_2 = \Delta/\sin \beta$ (δ_1 and δ_1' are the centering errors caused by the imprecision of manufacturing the jaw profile on one or the other of its sides, respectively).

Analysis of the constraints on the angle β with respect to the reliability of holding the component shows that $\beta \le 59°$ to 69° (constraint 1-1) (Figure 3). The centering error in the presence of imprecision in the manufacture of the profile on one side amounts to $\delta_1 \approx 1.4\Delta$. To obtain the same centering precision when there has been imprecision in manufacturing both sides, it is necessary that $\beta \ge 45°$. The optimum value of the angle β with respect to centering precision is 60°, with $\delta_1 = \delta_2 = 1.15\Delta$.
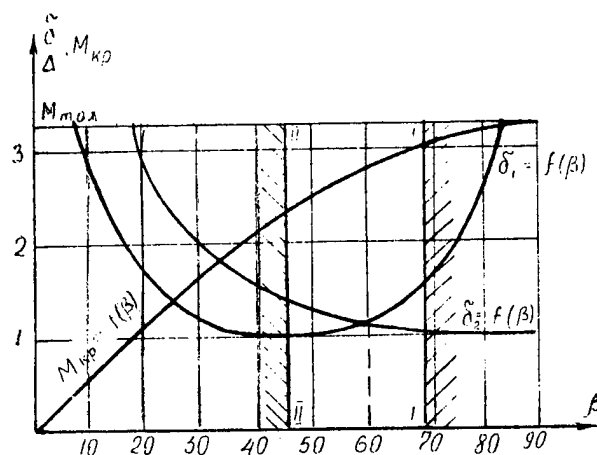
Figure 3.

The proposed method for numerically calculating and plotting the jaw profile of a wide-range centering gripping mechanism thus makes it possible to obtain a high centering precision with a wide range of change in components' diameters; expand the ranges of change of components' diameters, which is limited only by the gripping mechanism's design features; and optimize the

gripping mechanism's parameters with respect to minimizing the effect of the imprecision of the manufacture of the jaw profile, reducing the force on the gripping mechanism's drive, and reducing loose turning on the part of the jaws.

Bibliography

1. Kozyrev, Yu. G., "Promyshlennyye roboty: Spravochnik" [Industrial Robots: Manual], Moscow, Mashinostroyeniye, 1983, 376 pages.

UDC 658.512:621.002

Formation of Standardized Basic Structural Elements for Components in
Machining Process CAD System

[Article by P. A. Rudenko, candidate of technical sciences and professor, P.
N. Pavlenko, engineer, and N. M. Belyayev, engineer; first paragraph is
IZVESTIYA VYSSHIKH UCHEBNYKH ZAVEDENIY: MASHINOSTROYENIYE abstract]

[Text] This article examines the principles lying at the foundation of the
formation of a library of standardized basic structural elements for machine
building components. Algorithms are proposed for formalizing the processes
examined, and optimization related to creating and developing libraries of
standardized elements is performed.

At present decisions in machining process CAD systems are implemented by
methods of addressation and synthesis. Design procedures are formulated in
the process of examining and comparing a component and its elements with
standardized basic structural elements. The presence of a manufacturing
decision that can only be used unchanged during the design process is proposed
for each standardized basic structural element. Design decisions can only be
modified and individualized by using the synthesis method. Such subsystems
made up of libraries of standardized basic structural elements may be
considered knowledge bases.

The task of creating libraries of standardized basic structural elements and
manufacturing decisions faces all developers of machining process CAD systems.
At the same time there is the task of constantly filling such libraries with
new data appearing during the process of the machining process CAD system's
operation when there is a change in the product list at an enterprise. The
correctness of methods of formulating standardized basic structural elements
largely determines the efficiency of the functioning of the entire CAD system.
We will examine the problems of forming standardized basic structural
elements.

The set of components of an enterprise's product list may be represented in
the form of two subsets: components whose production has already been set up
and components that are in the stage of technological preparation of
production. A library of standardized basic structural elements and a

corresponding library of
manufacturing decisions is
constructed for the specified
subsets. Figure 1 represents the
process of the formation of these
libraries and shows the
correspondences between them.

Figure 1. Formation of libraries of
standardized basic structural
elements [YKTE] and manufacturing
decisions [TP]. (KTE = basic structural elements.)
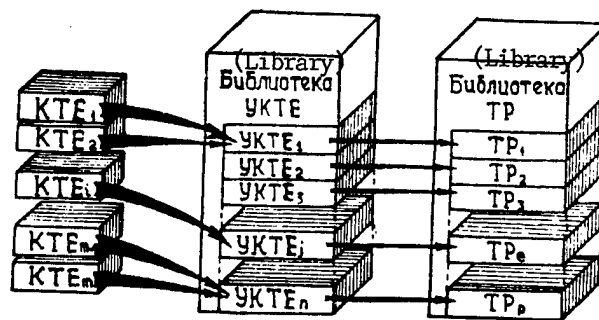
In accordance with the requirements of a structural systems approach, a
component may be described in terms of two sets: basic structural elements
forming a component and their structures. In turn, each basic structural
element may be described in terms of two subsets: sets of parameters and
their structural links. The adequacy of the model of a component constructed
on the basis of these subsets is achieved by selecting the segmentation level
of the of a component into elements and the completeness of the reflection of
information about these elements and and the structural links between them.[1]

To meet the requirements of the
structural approach, in accordance
with a previous work,[2] the basic
structural elements are divided into
levels when the model of a component
is constructed. The entire set of
basic structural elements forming a
component may then be represented by
joining subsets of elements
belonging to the respective levels
of the hierarchy (Figure 2).
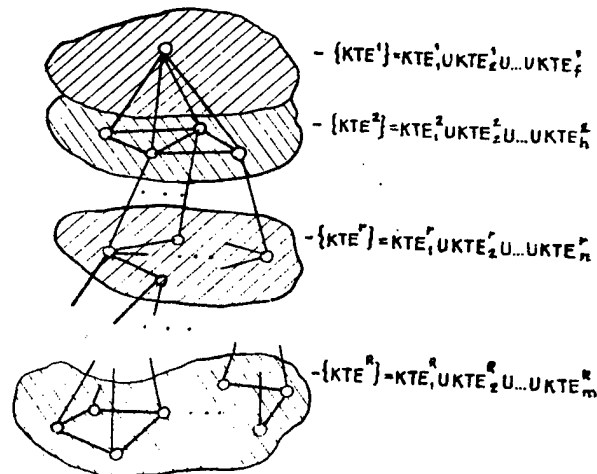
Figure 2. Structure of the
information model of a component
(KTE = basic structural element;
UKTE = standardized basic structural element).

To hasten sorting and selecting of data in modern CAD systems, the coding of
the basic structural elements is changed. In view of what has been said, the
model of a component may be presented in the form of the following expression:

(1)
$$D_i = \{K(E_t^r),\ KP(E_t^r),\ GKP(E_t^r),\ G(E_t^r)\,|\,t^r = 1,\ ...\ T^r,\ r = 1,\ ...,\ R\},$$

where D_i is the i-th component examined, $K(E_{tr})$ is the code of the element
$KP(E_{tr})$, $KP(E_{tr})$ is the set of parameters of the element E_{tr}, $G(E_{tr})$ are the
structural links of the elements E_{tr}, E_{tr} is the t-th basic structural element
belonging to the level r, and R is the number of levels.

In turn, the basic structural element of a component may be described in terms
of the expression

(2)
$$E_{t^r} = \{K(E_t^r),\ KP(E_t^r),\ GKP(E_{t^T})\}.$$

For a standardized basic structural element, the expression describing it is analogous to expression (2)

(3)
$$E_u(K) = \{K(E_u),\ KP(E_u),\ GKP(E_u)\},$$

where $E_u(K)$ is the standardized basic structural element with the code K, $KP(E_u)$ is the set of parameters of the element with the code $K(E_u)$, and $GKP(E_u)$ is the structure of the set of parameters of the element E_u.

The set of all standardized elements included in the library of standardized basic structural elements forms the set of standardized elements $\{E_u\}$. This set is initially formed on the basis of the set of components that have already been launched into production and is added to as new components are launched into production. A generalized algorithm for forming a set of standardized basic structural elements is presented below.

Step 1. For elements having one code, the subsets that are common regions for both the parameter sets and the structure of the parameter sets of the elements under examination are found

(4)
$$\{\overline{KP}(E_k)\} = \{KP(E_{k,1})\} \cap \ldots \cap \{KP(E_{k,i})\} \cap \ldots \cap \{KP(E_{k,A})\},$$

(5)
$$\{\overline{GKP}(E_k)\} = \{GKP(E_{k,1})\} \cap \ldots \cap \{GKP(E_{k,i})\} \cap \ldots \cap \{GKP(E_{k,A})\},$$

where $\{\overline{KP}(E_k)\}$ and $\{\overline{GKP}(E_k)\}$ are sets of common elements of the parameter sets and the structure of the parameter sets formed for elements (with the code K) of the components D_1, D_2, ..., D_A; $\{KP(E_k,i)\}$ is that set of parameters with the code K that belong to the component D_1; and $\{GKP(E_k,i)\}$ is the set of structural links of the set of parameters for those elements with the code K belonging to the component D_i.

Step 2. The original components of the set of parameters and its structure for each basic structural element having the given code are determined.

(6)
$$\triangle KP(E_{k,i}) = (\{\overline{KP}(E_k)\}\ U\ \{KP(E_{k,i})\}\setminus\{KP(E_{k,i})\},$$

(7)
$$\triangle GKP(E_{k,i}) = (\{\overline{GKP}(E_k)\}\ U\ \{GKP(E_{k,i})\}\setminus\{GKP(E_{k,i})\},$$

where $\triangle KP(E_k,i)$ and $\triangle GKP(E_k,i)$ are original components of the set and structure of the parameters for those elements of the code K belonging to the component D_i.

Step 3. The previously formed sets $\{\overline{KP}(E_k,i)\}$ and $\{\overline{GKP}(E_k,i)\}$ of the parameter sets for the standardized basic structural elements with the code under examination are supplemented with the resultant data, i.e., $\triangle KP(E_k,i)$ and $\triangle GKP(E_k,i)$

(8)
$$\{E_{u,k}\} = \begin{cases} \{\{\overline{KP}(E_k)\}\ U\ \{\triangle KP(F_{k,1})\ U\ \triangle KP(E_{k,2})\ U\ldots UKP(E_{k,A})\} \\ \{\overline{GKP}(E_k)\}\ U\ \{\triangle GKP(E_{k,1})\ U\triangle GKP(E_{k,2})\ U\ldots UGKP(E_{k,A})\}. \end{cases}$$

37

Step 4. We obtain the standardized basic structural elements with the given code by processing information regarding the list of components manufactured within the range of one code.

Step 5. As a result of the formation of standardized basic structural elements with respect to all codes encountered in the list of components, it is possible to produce a library of standardized basic structural elements

$$(9) \qquad \{E_u\} = \{E_{u,1}\} \ U \ \{E_{u,2}\} \ U \ \{E_{u,N}\},$$

where N is the number of types of component elements throughout the entire product list.

When the product list changes, a search is conducted for new components of the parameter set and its structure for each element code. The resultant data are used to supplement the information files of standardized basic structural elements describing the set of parameters and its structure. In the case where a new code is encountered, it is processed in accordance with the algorithm for forming a standardized element that was examined above.

The algorithms presented make it possible to formalize the process of forming standardized basic structural elements. Examining the formalized technique for forming them makes it possible to optimize the job of creating and developing libraries of standardized elements.

Conclusions

1. A method of creating a library of standardized basic structural elements has been developed on the basis of analyzing a component and the links between the elements forming it.

2. The distinction of this method is that it affords the capability of self-organization of libraries of standardized basic structural element during the process of their use.

Bibliography

1. Rudenko, P. A., and Pavlenko, A. N., "Metodika avtomatizirovannogo proyektirovaniya struktury tekhnologicheskogo protsessa. Inf. listok ChnMTsNTI" [Method of CAD of Structure of Manufacturing Process. ChNMTsNTI Information Sheet], Chernigov, No 89-007, 1989, 4 pages.

2. Didenko, V. P., Yevgenev, G. B., and Kuznetsov, I. I., "Systems Approach in Analyzing Structure of Automated Processes and Systems," in "Avtomatizirovannoye proyektirovaniye i proizvodstvo v mashinostroyenii" [CAD and Production in Machine Building], by Yu. M. Solomentsev, V. G. Mitrofanov, A. F. Prokhorov, et al., ed. by Yu. M. Solomentsev and V. G. Mitrofanov, Moscow, Mashinostroyeniye, 1986, pp 53-61.

UDC 621.791.75:681.3.06

Computer Calculation of Mode for Arc Welding Butt Joints With Beveling of Edges

[Article by Ye. B. Maslova, student, A. M. Rybachuk, docent, and A. V. Konovalov, engineer; first paragraph is IZVESTIYA VYSSHIKH UCHEBNYKH ZAVEDENIY: MASHINOSTROYENIYE abstract]

[Text] This article proposes an algorithm for selecting the optimum method of welding and calculating a welding mode with the necessary surfacing area and maximum penetration capability.

When welding butt joints 20 to 40 mm thick it becomes necessary to select that welding method and mode ensuring filling of the bevel and complete fusion of the cross section. Automatic submerged-arc welding and CO_2 shielded-arc welding are most suitable for products made of low-carbon steel. Experimental analysis requires great expenditures of labor, time, and materials. It is proposed that the task be performed by using a computer and that subsequent experimentation only refine the results obtained.

The work was performed for a specific product -- a cylindrical shell made of low-carbon steel and with an outer diameter of 515 mm and a thickness of 34 mm. The shell was welded with a quality lengthwise seam. The term "quality" is understood to mean complete fusion of the cross section and achievement of the required fusion area. Owing to the uneven deformation of the metal during roll forming, the spread of the edges in the joint has a variable value for different shells, which in turn makes it necessary to weld different amounts of metal into the bevel. The bevel has a nonstandard V-shaped form with an angle that changes along the length of the joint and that differs in different products. The purpose of this work is to select that welding mode ensuring filling of the bevel and complete fusion of the cross section in submerged-arc welding and CO_2 shielded-arc welding.

To obtain the source data, the spread of the edges y (Figure 1) was measured in three different cross sections along the length of the joint in 35 products. Values of the mean square deviation of the spread of the edges of $\sigma_1 = 1.25$, $\sigma_2 = 1.26$, and $\sigma_3 = 1.03$ were obtained for each cross section separately. These deviations were obtained in accordance with the following formula

$$\sigma = \sqrt{\frac{\sum\limits_{i=1}^{n}(y_i - \bar{y})^2}{n-1}} ,$$

where n is the number of measurements and y and y_i are the mean and running values of the spread of the edges.

Figure 1. Joint of a shell (a) and diagram of the arrangement of the cross sections in which the overlapping of the edges were measured.

a)　　　　　　б)
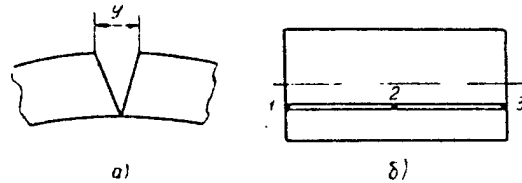
For each cross section, we find the variance in accordance with the formula $D = \sigma^2$: $\sigma_1^2 = 1.57$, $\sigma_2^2 = 1.61$, and $\sigma_3^2 = 1.07$.

Estimating the uniformity of the variances in accordance with Fisher's criterion showed that all of the values of the spread of the edge for the three different cross sections may be combined into one general set, i.e., the variances are uniform. A mathematical expectation of the value of the spread of the edges in the joint of M(y) = 14 mm was calculated for the general set. Statistical processing[2] showed that the distribution of the values of the spread of the edges is subjected to a normal gaussian distribution law with the following parameters: a = 14 and σ = 1.26.

Figure 2 presents a histogram whose ordinate represents the relative frequencies h of the appearance of one value for the spread of the edges or another in the grouping intervals and whose abscissa represents the bounds of these intervals. Figure 2 shows a normal distribution curve approximating the histogram. The same statistical calculation results may be obtained by using a computer.
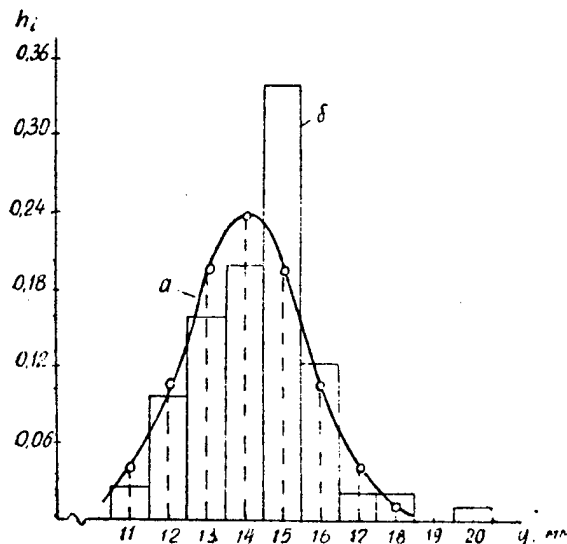
Figure 2. Results of statistical processing: a, curve with a normal distribution; b, histogram.

A program to calculate modes of submerged-arc welding and CO_2 shielded-arc welding in accordance with the existing methods[1] was compiled to select the welding method and determine that welding mode providing the required depth of fusion. The constant thermophysical coefficients are selected from a previously formulated data file. Input from a display screen are the type of welding (CO_2 shielded-arc welding or submerged-arc welding); the thickness of the metal being welded; the bounds of the measurements of the welding current I, the welding speed V_B, the electrode diameter d_E, the electrode tip b, and the bevel area; the surfacing error; and the measurement

40

intervals of the current, electrode diameter, throat capacity, and welding speed.

The calculation is reduced to determining that welding mode during which we achieve a balance between the volumes of the bevel and surfaced metal given different combinations of welding speed, arc voltage, and electrode diameter and tip.

Figure 3.   Flowchart of the program.

Key:

1. Beginning
2. Input source data
3. Modification of values of mode parameters
4. Determination of surfacing area
5. Bevel is filled
6. Determination of depth of fusion H
7. H > Hmax
8. Preservation of running parameters
9. Hmax = H
10. Print parameters of mode selected
11. End
12. No
13. Yes

The calculation algorithm is presented in the form of a flowchart (Figure 3). The calculation begins with a calculation of the fusion coefficient:

(1) $\alpha_p = \alpha'_p + \Delta\alpha_p.$

In the case of welding using a direct current with reverse polarity

$$\alpha'_p = 11{,}6 \pm 0{,}4 \ \text{r/A}\cdot\text{ч},$$
$$\Delta\alpha_p = 3600 \ (Q_{nn}/q_\vartheta I).$$

The value of Q_{nn} is calculated in accordance with the formula

(2) $Q_{nn} = 0{,}1884 j^2 \rho_0 d^2 \left[\dfrac{V_\vartheta}{a\,\alpha\beta} (e^{-\rho_\vartheta b} - 1) - \dfrac{\alpha (T_{nn} - T_0)}{p_1} \right].$

The coefficients ß, p1, and p2 are calculated in accordance with the formulas

(3) $\beta = 0{,}576 j^2 \rho_0 / ac\gamma,$

(4) $p_{1,2} = -\dfrac{V_\vartheta}{2a} \pm \sqrt{\left(\dfrac{V_\vartheta}{2a}\right)^2 - \alpha\beta,}$

41
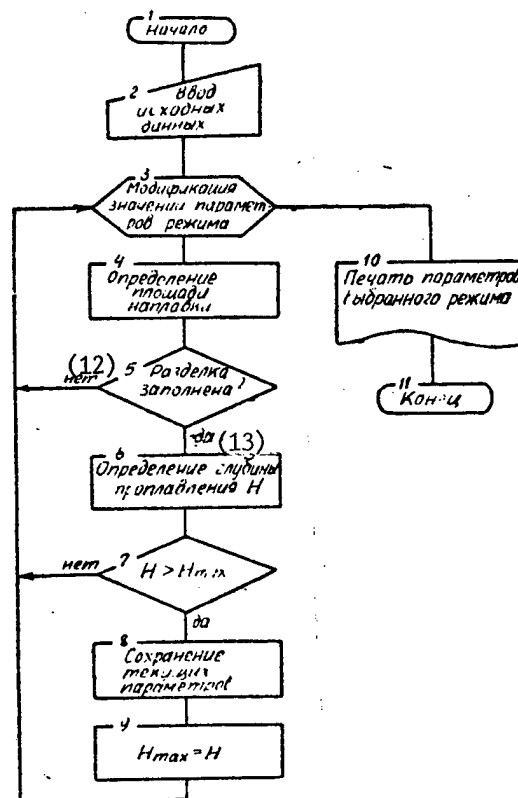
where V_E is the relative speed at which the wire is fed (m/hr),

(5)
$$V_\mathfrak{s} = \alpha'_p j / 3600\gamma;$$

and j is the current density (A/mm²)

$$j = I/F_\mathfrak{s}, \quad F_\mathfrak{s} = \pi d_\mathfrak{s}^2 / 4.$$

The next step is that of determining the surfacing area F_H. We will estimate the losses due to melting and spattering. For welding in CO_2,

(6)
$$\Psi_\text{н} = -4{,}72 + 0{,}176j - 0{,}000448j,$$

for submerged-arc welding $\Psi_\text{П} = 0.03$ (%).

Next, we fine the rate at which the electrode wire is fed (m/hr):

(7)
$$V_\text{пп} = \alpha_p I / \gamma F_\mathfrak{s},$$

(8)
$$F_\text{н} = (F_\mathfrak{s} V_\text{пп} / V_\text{св})(\alpha_\text{н}/\alpha_\text{п}),$$

where $\alpha_H = \alpha_p(1 - (\Psi_\pi/100))$ for welding in CO_2 and $\alpha_H = \alpha_p(1 - 0.03)$ for submerged-arc welding.

The surfacing area is calculated within the cycles by a one-by-one trial of the values of the welding current, welding speed, and diameter and tip of the electrode (Figure 3). As soon as the difference between the values of the surfacing area and the bevel area turns out to be less than the allowable surfacing error ε, the calculation of the surfacing area is halted. It is advisable to determine the modes for the maximum bevel area value. The calculation results in that range of combinations of mode parameters providing the necessary surfacing area. This is because complete depth of fusion in so narrow a bevel is not possible during any welding mode. The fusion capacity of the modes was compared for the case of surfacing. The depth of fusion is determined in accordance with the formulas

(9) for submerged-arc welding $H_\text{пр} = 0{,}156 \sqrt{q/V_\text{св}\Psi_\text{пр}}$

(10) for CO_2 shielded-arc welding $H_\text{пр} = 0{,}165 \sqrt{q/V_\text{св}\Psi_\text{пр}}$

where $q = IU_D\eta_I$ and $\Psi_{\pi p} = k'(19 - 0.01I)(d_E U_D/I)$.

With a current density of $j < 120$ A/mm², $k' = 0.282j^{0.1925}$ during welding with a direct current having direct polarity, and $k' = 0.367j^{0.1925}$ during welding with a direct current having reverse polarity. When $j \geq 120$ A/mm², $k' = 0.92$ with a current having direct polarity, and $k' = 1.12$ with a current having reverse polarity.

After having determined the depth of fusion (in accordance with (9) and (10)) for the possible welding modes, we select the one mode with the maximum depth of fusion (Figure 3). The program developed thus makes it possible to select

the method and calculate the mode of welding providing the required surfacing area and the maximum fusion capacity.

Bibliography

1. Akulov, A. I., Belchuk, G. A., and Demintsevich, V. P., "Tekhnologiya i oborudovaniye svarki plavleniyem. Uchebnik dlya studentov vtuzov" [Technology and Equipment for Fusion Welding. Textbook for Students at Higher Technical Schools], Moscow, Mashinostroyeniye, 1977, 432 pages.

2. Maslov, B. G., "Nerazrushayushchiye methody kontrolya kachestva svarnykh shvov" [Nondestructive Methods of Testing Quality of Welds], Moscow, Mashinostroyeniye, 1976, 72 pages.

UDC 621.9

Constructing Matrix Models of Precision of Manufacturing Processes

[Article by L. K. Sizenov, doctor of technical sciences, and A. A. Gusev, candidate of technical sciences; first paragraph is IZVESTIYA VYSSHIKH UCHEBNYKH ZAVEDENIY: MASHINOSTROYENIYE abstract]

[Text] This article examines methods of constructing multidimensional multifactoral mathematical models of the precision of a set of interconnected operations entailed in manufacturing processes as the foundation of forecasting and controlling production quality.

To model manufacturing processes we will introduce the following spaces into our examination. The factor space of a process consisting of n operations is the linear space of the vectors whose coordinates are the errors in the initial factors of the blanks and the parameters of the manufacturing systems in which the operations are implemented. In accordance with the linear dependence of the factors, it may be represented in the form of the direct sum of n+1 spaces $U_0 \oplus V_1 \oplus \ldots \oplus V_n$, where U_0 is the space of the arbitrary vector of the input variables of the initial blanks (error in dimensions, deviations in shape, microgeometry, hardness, etc.); V_i is the space of the arbitrary vector of the manufacturing system's input variables (rigidity, tool wear, temperature deformation, adjustment error, etc.) affecting the output variables of the i-th manufacturing operation (i = 1, ..., n) characterizing the parameters of the quality of the blanks undergoing machining (error in dimensions, deviations of the shape, arrangement of the surfaces, waviness, etc.).

Let the parameters of the component's quality that changed or that arose at the outlet from the i-th operation form the arbitrary vector $\vec{z}_i$ varying in the space U_i. This i-th operation may be represented as a linear heterogeneous transform of the spaces

$$U_{i-1} \oplus V_i \oplus \ldots \oplus V_n \rightarrow U_i \oplus V_{i+1} \oplus \ldots \oplus V_n,$$

that any vector

$$\vec{x}_{i-1} \in U_{i-1} \oplus V_i \oplus \ldots \oplus V_n,$$

transforms into the vector

$$\vec{x_i} \in U_i \oplus V_{i+1} \oplus \dots \oplus V_n$$

in accordance with the formula

(1) $$\vec{x_i} = A_{i_0} + A_i\vec{x_{i-1}} \quad (i = 1, \dots, n),$$

where A_{i0} is the matrix column of free terms and A_i is the matrix of the transfer coefficients.[1] For convenience of writing, we will complement the vector $\vec{x_i}$ with a fictitious variable to the vector

(2) $$\tilde{\vec{x_i}} = \left(\frac{x_{i_0}}{\vec{x_i}} \right) \quad (i = 0, 1, \dots, n)$$

and will introduce the new matrix

(3) $$\tilde{A_i} = \left(\begin{array}{c|c} 1 & 0 \ 0 \dots 0 \\ \hline A_{i_0} & A_i \end{array} \right) \quad (i = 1, \dots, n).$$

By taking (2) and (3) into account, we may write transform (1) in homogeneous form

(4) $$\tilde{\vec{x_i}} = \tilde{A_i}\,\tilde{\vec{x_{i-1}}}.$$

Let us write the leveling of the constraint on the output quality parameters of components from the i-th and j-th operations (j < i) in homogeneous form

(5) $$\tilde{\vec{x_i}} = \tilde{A_i} \dots \tilde{A_{j+1}}\tilde{\vec{x_j}} \quad (i > j = 0, 1, \dots, n)$$

or in heterogeneous form

(6) $$\vec{x_i} = A_{i_0} + A_i A_{i-1,0} + A_i A_{i-1} A_{i-2,0} + \dots + A_i \cdot \dots \cdot A_{j+1}\vec{x_j}.$$

A manufacturing process may be represented in terms of a graph (Figure 1) illustrating the model in scalar form (Figure 1a) or in terms of a heterogeneous matrix (Figure 1b and (6)) or homogeneous matrix (Figure 1c and (5)). The nodes of the graph shown in Figure 1c that are indexed by vectors are the output quality parameters of the process, whereas the ribs are transfer matrices. The path from node $\tilde{\vec{x_j}}$ to node $\tilde{\vec{x_i}}$ (i > j) drawn along the graph in the direction of the orientation designates the transition from the properties $\tilde{\vec{x_j}}$ to the quality parameters $\tilde{\vec{x_i}}$ in accordance with (5).

By applying the operation of mathematical expectation to matrix equation (5), we obtain

45

(7)
$$\tilde{m}_{\vec{\tilde{x}}_i} = \tilde{A}_i, ..., \tilde{A}_{j+1}\tilde{m}_{\vec{\tilde{x}}_j} \quad (i > j = 0, 1 ..., n).$$
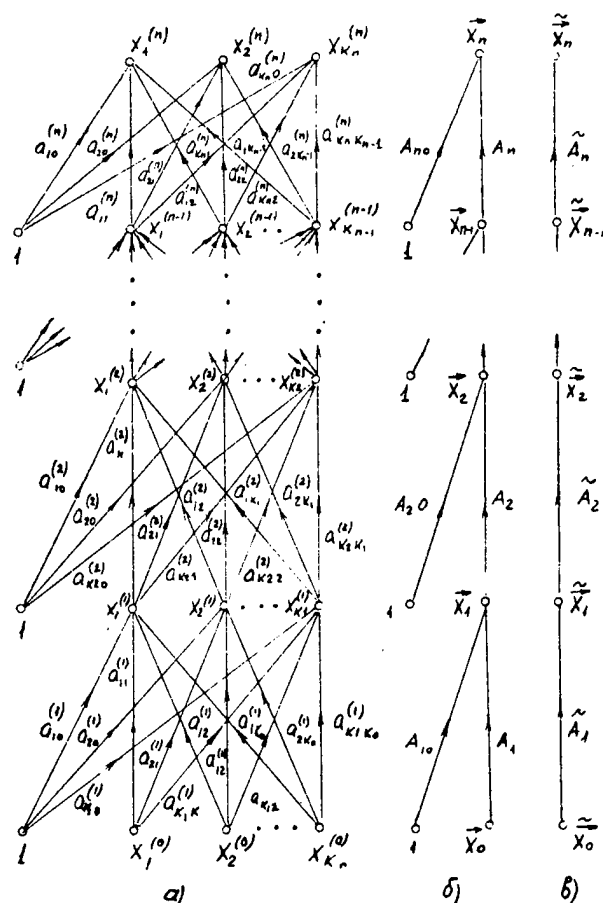

Figure 1. Graph of a manufacturing process: a, for scalar writing of the constraint equation; b, for matrix writing of heterogeneous constraint equations (6); c, for matrix writing of homogeneous constraint equations (5).

The correlation matrix of the arbitrary vector of the output quality parameters $\vec{x}_i$ derived as a result of linear transformation (5) of the vector x_j of the original manufacturing factors is determined in accordance with the formula

(8)
$$K\tilde{\vec{x}}_i \tilde{\vec{x}}_i = \tilde{A}_i \cdot ... \cdot \tilde{A}_{j+1} K\vec{\tilde{x}}_j \vec{\tilde{x}}_j \tilde{A}_{j+1} \cdot ... \cdot \tilde{A}_i' \quad (i > j = 0, 1, ..., n).$$

For heterogeneous constraint equations (6), we may write the following instead of the probability characteristics (7) and (8):

(9)
$$\vec{m}_{\vec{x}_i} = A_{i_0} + A_i A_{i-1.0} + ... + A_i \cdot ... \cdot A_{j+2} A_{j+1.0} + A_i \cdot ... \cdot A_{i+1} m_{\vec{x}_j}$$

(10)
$$K\vec{x}_i \vec{x}_i = A_i \cdot ... A_{j+1} K\vec{x}_j \vec{x}_j A'_{j+1} \cdot ... \cdot A_j' \quad (i > j = 0, 1, ..., n).$$

By isolating the diagonal elements in correlation matrix (10), we obtain the variance of the output quality parameters of the i-th operation

$$D^{(i)}_{x_k} = A_{i_k} A_{i-1} \cdot \ldots \cdot A_{j+1} K_{\overrightarrow{x_j}\,\overrightarrow{x_j}} A'_{j+1} \cdot \ldots \cdot A'_{i-1} A'_{i_k}$$

(11)

$$(i = 1, 2, \ldots, n; \quad k = (1, 2, \ldots, s_k).$$

where $D_{xk}^{(i)}$ is the variance of the k-th output of the i-th operation and A_{ik} is the k-th line of the matrix A_i.

By switching in (11) from the variances to the stray fields of the errors, we derive a constraint equation for the stray fields of the output quality parameters of the i-th and j-th operations

$$\Delta^{(i)}_{x_k} = k^{-1}_{x_k}(i)\,(A_{i_k} A_{i-1} \cdot \ldots \cdot A_{j+1} k \overrightarrow{x_j} \Delta \overrightarrow{x_j} \times$$

(12)

$$\times K_{\overrightarrow{x_j}\,\overrightarrow{x_j}} \Delta \overrightarrow{x_j} k \overrightarrow{x_j} A'_{j+1} \cdot \ldots \cdot A'_{i-1} A_{i_k})^{1/2}$$

$$(i > j, \; j = 0, 1, \ldots, n-1; \; i = 1, \ldots, n; \; k = 1, \ldots, s_i),$$

where $\Delta_{xk}^{(i)}$ and $k_{xk}^{(i)}$ are the stray field and coefficient of the respective scatter of the k-th output quality parameter of the i-th operation and $\Delta\overrightarrow{x}_j$ and $k\overrightarrow{x}_j$ are diagonal matrices of the stray fields and the coefficients of the relative scatter of the components of the vector $\overrightarrow{x}_j$.

Table 1. Construction of a mathematical model of the precision of an automatic line.

(1) Этапы технологического процесса	(2) Точностные характеристики		(3) Коэффициент корреляции	(4) Передаточные характеристики [1]	(5) Дисперсии собственных погрешностей обработки [1]
	m_{x_i}, мм	σ_{x_i}, мкм (μ m)	$r_{x_i\,x_{i-1}}$	$a_i = r_{x_i\,x_{i-1}} \dfrac{\sigma_{x_i}}{\sigma_{x_{i-1}}}$ $ai_0 = m_{x_i} - a_i m_{x_{i-1}}$	$\sigma^2_{x_i\,x_{i-1}} = \sigma^2_{x_i}(1 - r^2_{x_i x_{i-1}}),$ мкм^2 (μ m^2)
Заготовка $(i=0)$ (6)	14	100	—	—	—
Токарная автоматная обработка $(i=1)$ (7)	10,3	10	0,5	$a_1 = 0,5\dfrac{10}{100} = 0,05$ $a_{10} = 10,3 - 0,005 \cdot 14 = 9,6$	$\sigma^2_{x_1 x_0} = 10^2(1-0,5^2) = 75$
Бесцентрово-шлифо-вальная обработка $(i=2)$ (8)	9,983	4	0,4	$a_2 = 0,4\dfrac{4}{10} = 0,16$ $a_{20} = 9,983 - 0,16 \cdot 10,3 = 8,335$	$\sigma^2_{x_1 x_2} = 4^2(1-0,4^2) = 13,44$

1. Steps in the manufacturing process
2. Precision characteristics
3. Correlation coefficient
4. Transfer characteristics[1]

5. Variance of the inherent machining errors[1]
6. Blank (i = 0)
7. Automatic turning (i = 1)
8. Eccentric grinding (i = 2)

As an example, let us examine the construction of a mathematical model of the precision of machining rollers on interconnected corridors of an automatic line. Investigation of a batch of blanks throughout all stages of the manufacturing process resulted in the precision characteristics m_{xi} and σ_{xi} and establishment of linear correlation links r_{xixi-1} between them. Table 1 presents the sequence of the calculations.

The mathematical model of the machining precision is as follows:

$$m_{x_2} = a_{20} + a_2 a_{10} + a_1 a_2 m_{x_0} = 9,871 + 0,008 m_{x_0};$$
$$\sigma^2_{x_2} = \sigma^2_{x_2 x_1} + a^2 \sigma_{x_1 x_0} + a^2_2 a^2_2 \sigma^2_{x_0} = 15,36 + 6,4 \cdot 10^{-5} \sigma^2_{x_0}.$$

Analyzing mathematical models permits well-founded designation of the requirements regarding a blank's precision and, in some cases, expands the tolerances for its manufacture. This in turn improves the technical and economic indicators of the manufacturing process.

A method of constructing matrix models that permits a comprehensive analysis of the precision of an entire manufacturing process with an allowance for the effect of an entire set of factor and examination of all of the principal quality characteristics of components has thus been developed.

Bibliography

1. Gavrilov, A. N., ed., "Tochnost proizvodstva v mashinostroyenii i priborostroyenii" [Precision of Manufacturing in Machine Building and Instrument Making], Moscow, Mashinostroyeniye, 1973, 567 pages.

2. Kalskiy, A. M., "Tekhnologicheskoye obespecheniye nadezhnosti vysokotochnykh detaley mashin" [Technological Support of Reliability of High-Precision Machinery Components], Moscow, Mashinostroyeniye, 1975, 223 pages.

- END -

This is a U.S. Goveri .... the
policies, views, or attitudes of the U.S. Government. Users of this publication may
cite FBIS or JPRS provided they do so in a manner clearly identifying them as the
secondary source.

Foreign Broadcast Information Service (FBIS) and Joint Publications Research Service (JPRS)
publications contain political, military, economic, environmental, and sociological news, commentary,
and other information, as well as scientific and technical data and reports. All information has been
obtained from foreign radio and television broadcasts, news agency transmissions, newspapers, books,
and periodicals. Items generally are processed from the first or best available sources. It should not be
inferred that they have been disseminated only in the medium, in the language, or to the area indicated.
Items from foreign language sources are translated; those from English-language sources are tran-
scribed. Except for excluding certain diacritics, FBIS renders personal and place-names in accordance
with the romanization systems approved for U.S. Government publications by the U.S. Board of
Geographic Names.

Headlines, editorial reports, and material enclosed in brackets [ ] are supplied by FBIS/JPRS.
Processing indicators such as [Text] or [Excerpts] in the first line of each item indicate how the
information was processed from the original. Unfamiliar names rendered phonetically are enclosed in
parentheses. Words or names preceded by a question mark and enclosed in parentheses were not clear
from the original source but have been supplied as appropriate to the context. Other unattributed
parenthetical notes within the body of an item originate with the source. Times within items are as given
by the source. Passages in boldface or italics are as published.

SUBSCRIPTION/PROCUREMENT INFORMATION

The FBIS DAILY REPORT contains current news
and information and is published Monday through
Friday in eight volumes: China, East Europe, Soviet
Union, East Asia, Near East & South Asia, Sub-
Saharan Africa, Latin America, and West Europe.
Supplements to the DAILY REPORTs may also be
available periodically and will be distributed to regular
DAILY REPORT subscribers. JPRS publications, which
include approximately 50 regional, worldwide, and
topical reports, generally contain less time-sensitive
information and are published periodically.

Current DAILY REPORTs and JPRS publications are
listed in *Government Reports Announcements* issued
semimonthly by the National Technical Information
Service (NTIS), 5285 Port Royal Road, Springfield,
Virginia 22161 and the *Monthly Catalog of U.S. Gov-
ernment Publications* issued by the Superintendent of
Documents, U.S. Government Printing Office, Wash-
ington, D.C. 20402.

The public may subscribe to either hardcover or
microfiche versions of the DAILY REPORTs and JPRS
publications through NTIS at the above address or by
calling (703) 487-4630. Subscription rates will be

provided by NTIS upon request. Subscriptions are
available outside the United States from NTIS or
appointed foreign dealers. New subscribers should
expect a 30-day delay in receipt of the first issue.

U.S. Government offices may obtain subscrip-
tions to the DAILY REPORTs or JPRS publications
(hardcover or microfiche) at no charge through their
sponsoring organizations. For additional information
or assistance, call FBIS, (202) 338-6735,or write
to P.O. Box 2604, Washington, D.C. 20013.
Department of Defense consumers are required to
submit requests through appropriate command val-
idation channels to DIA, RTS-2C, Washington, D.C.
20301. (Telephone: (202) 373-3771, Autovon:
243-3771.)

Back issues or single copies of the DAILY
REPORTs and JPRS publications are not available.
Both the DAILY REPORTs and the JPRS publications
are on file for public reference at the Library of
Congress and at many Federal Depository Libraries.
Reference copies may also be seen at many public
and university libraries throughout the United
States.